Transport of spin qubits with donor chains under realistic experimental conditions

Fahd A. Mohiyaddin, Rachpon Kalra, Arne Laucht, Rajib Rahman, Gerhard Klimeck, and Andrea Morello

Transport of Spin Qubits with Donor Chains under Realistic Experimental Conditions

Fahd A. Mohiyaddin,[1] Rachpon Kalra,[1] Arne Laucht,[1] Rajib Rahman,[2] Gerhard Klimeck,[2] and Andrea Morello[1]

[1]*Centre for Quantum Computation and Communication Technology,*
School of Electrical Engineering and Telecommunications, UNSW Australia, Sydney NSW 2052, Australia
[2]*Network for Computational Nanotechnology, Purdue University, West Lafayette, IN 47907, USA*
(Dated: May 23, 2016)

The ability to transport quantum information across some distance can facilitate the design and operation of a quantum processor. One-dimensional spin chains provide a compact platform to realize scalable spin transport for a solid-state quantum computer. Here, we model odd-sized donor chains in silicon under a range of experimental non-idealities, including variability of donor position within the chain. We show that the tolerance against donor placement inaccuracies is greatly improved by operating the spin chain in a mode where the electrons are confined at the $Si-SiO_2$ interface. We then estimate the required timescales and exchange couplings, and the level of noise that can be tolerated to achieve high fidelity transport. We also propose a protocol to calibrate and initialize the chain, thereby providing a complete guideline for realizing a functional donor chain and utilizing it for spin transport.

Among the leading physical platforms for the practical implementation of quantum computers, donor spins in silicon[1] provide extremely long coherence times[2,3] combined with the compatibility with industry-standard fabrication techniques. The last five years have witnessed several experimental milestones in the quest to build a prototype of a donor-based silicon quantum computer. The essential operations of reading out and controlling the spin state of both the electron and nuclear spins of a single implanted ^{31}P donor were demonstrated in a gated nanostructure[4–6]. The spin coherence times of the donor electron and nuclear spin qubits in functional nanostructures reached 0.5 s and 30 s, respectively, with state-of-the-art material purification and advanced filtering techniques[7]. The scale up of these devices has remained a challenge, although important advancements have been made. Exchange-coupled donor pairs in silicon have been observed[8,9] and a two-qubit logic gate has been demonstrated with quantum dots in a similar nanostructure[10]. Fabrication based on scanning tunneling microscope (STM) lithography allows for donor incorporation with near-atomic precision[11].

Beyond the one- and two-qubit logic gates, which can be achieved using short-range interactions and global control fields, the construction of a large-scale quantum computer can greatly benefit from the ability to transport the qubit states across large distances. Even in dense architectures such as the surface code, it is known that long-distance links can help achieving exceptionally high fault-tolerant thresholds[12]. Moreover, they can simplify the layout of a quantum processor by allowing extra space between the physical qubits to accommodate control electronics and other components.

Several proposals outline how the spin-carrying electron itself can be transported, whether by shuttling its confinement potential[13], or by adiabatic passage[14,15]. Other schemes involve spin-to-spin coupling between electrons such that transport is essentially achieved via a SWAP operation. This may come from direct exchange coupling, magnetic dipolar interaction[16,17], elec-

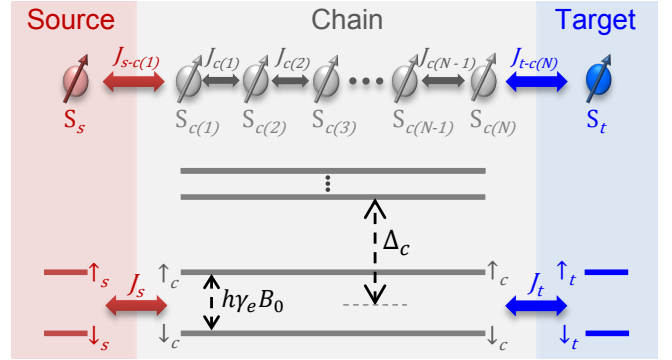FIG. 1. (Color online) Schematic of a spin chain (gray) where the spins at the edges ($S_{c(1)}$ and $S_{c(N)}$) are exchange-coupled to source and target qubits (S_s and S_t). When $\Delta_c \gg h\gamma_e B_0$, the chain forms an extended qubit, allowing spin transport from the source to the target. The magnitude of the effective coupling between the chain and source qubits, J_s, approaches $J_{s-c(1)}/\sqrt{N}$ for large N[24].

tric dipoles[18], or a coupling mediated via an intermediate quantum dot[19], a ferromagnet[20] or a resonant cavity[18,21,22].

One-dimensional spin chains have been proposed as a compact medium to couple distant spin qubits[23–27]. If the number of spins in the chain is odd and the spin-spin interactions within the chain are very strong, the chain effectively behaves like a spatially extended spin-1/2 qubit[28,29]. Therefore, the chain can serve as an intermediary qubit, providing a link between two qubits that are exchange coupled to either end of the chain, as shown in Figure 1. The spin state of the source can thus be transported first to the chain and then to the target qubit through sequential SWAP operations[24,30], which require precisely timed control of the source-chain and chain-target exchange couplings. An alternative transport protocol was recently described by Oh *et al.*[31], where the chain qubit is used to mediate an adiabatic state

transfer from source to target. The adiabatic nature of the protocol allows the transport to be extremely robust against timing jitter and other experimental imperfections.

Recent works have also investigated the use of an even-sized chain to couple two distant qubits[25,26]. The ground state of such a chain is a spin-zero singlet state, and therefore cannot be thought of as an extended qubit that couples to source and target. However, this spin-zero even-number chain can mediate a second-order coupling between two qubits exchange-coupled to either end of the chain. In this scenario, one effectively finds a single super-exchange coupling, linking directly the source to target qubit. This can be used for SWAP operations between source and target, with the caveat of their sensitivity to timing and other imperfections. The adiabatic transport protocol cannot be implemented on even-number chains, since it requires the use of an intermediary qubit.

Earlier theoretical work on spin chains[24–27] has given general guidelines on design rules and operation schemes for their use in quantum information processing. However, the practical implementation of a spin chain requires a system-specific appraisal of its physical properties and parameters, and a careful analysis of the manufacturability, error rate and speed of operation under realistic experimental conditions. Here, we analyze the suitability of donor chains for the transport of spin qubits in silicon. We consider exclusively odd-sized chains in order to enable the adiabatic transport protocol[31] which, as we will show, is highly robust to experimental errors.

The paper is organized as follows. In Section I, we outline the requirements for a donor chain to form the desired extended qubit and address the precision with which the donors need to be positioned. In Section II, we detail a protocol to calibrate the chain for transport. Finally, in Section III, we assess the fidelity of the adiabatic transport protocol[31] in the presence of magnetic and electrical noise, and with limited tunability of exchange couplings. Our results therefore provide a complete guideline for realizing a functional donor chain and utilizing it for spin transport.

I. CONSTRUCTION OF A DONOR CHAIN

We begin our analysis by considering a chain solely made up of electrons, and will only include the donor nuclei later in Section I B. The spin Hamiltonian for an odd number N of electrons with nearest-neighbor exchange couplings $J_{c(i)}$ in an externally applied static magnetic field B_0 is:

$$H_{c_e} = h\gamma_e B_0 \sum_{i=1}^{N} \frac{\sigma_{z,c(i)}}{2} + \sum_{i=1}^{N-1} J_{c(i)} \frac{\boldsymbol{\sigma}_{c(i)}}{2} \cdot \frac{\boldsymbol{\sigma}_{c(i+1)}}{2}, \quad (1)$$

where $\gamma_e \approx 28$ GHz/T is the gyromagnetic ratio of the electron. $\boldsymbol{\sigma}_{c(i)}$ is the vector Pauli operator for the

i^{th} electron spin in the chain and $\sigma_{z,c(i)}$ is the Pauli z-operator for the i-th spin, with z defined as the direction of the external field B_0. For example, for a chain with $N = 3$, $\sigma_{z,c(2)} = I_2 \otimes \sigma_z \otimes I_2$, where σ_z is the Pauli z-matrix, and I_2 is the 2×2 identity matrix.

The energy spectrum of an odd-number chain consists of a low-energy doublet of states, separated from the nearest excited states by a gap Δ_c (see Figure 1), that depends on the intra-chain exchange interaction strengths $J_{c(i)}$. The chain can be treated as an effective two-level system, i.e. a spin-1/2 qubit, under the condition[24]

$$\Delta_c \gg h\gamma_e B_0 \qquad (2)$$

where $h\gamma_e B_0$ is the Zeeman splitting of the ground doublet. Therefore we label the two lowest energy states of the chain as $|\uparrow_c\rangle$ and $|\downarrow_c\rangle$. Assuming $J_{c(i)} = J_c \ \forall \ i$, Δ_c is given by[29]

$$\Delta_c \approx \frac{J_c \pi^2}{2N} \qquad (3)$$

Notice that Δ_c is inversely proportional to the number of spins in the chain. If the intra-chain exchange couplings are not all equal, Δ_c needs to be calculated from the numerical diagonalization of Equation 1. One typically finds that, with inhomogeneous $J_{c(i)}$, Δ_c is mostly limited by the weaker couplings within the chain. Regardless of the details of the intra-chain couplings, the chain will function as an extended qubit provided the condition in Equation 2 is satisfied. The key point in practice is that the chain serves as an effective spin-1/2 as long as $J_{c(i)} \gg h\gamma_e B_0 \ \forall \ i$.

Two factors influence the choice of external magnetic field B_0. In donor systems, B_0 serves the purpose of disentangling the electron and the nuclear spins, which are coupled by the hyperfine interaction A. In the example of ^{31}P in silicon, the hyperfine coupling is $A/h \approx 117$ MHz[32]. The eigenstates of the ^{31}P spin Hamiltonian are approximate tensor products of the electron and nuclear states[33] provided $h\gamma_e B_0 \gg A$, thus requiring a minimum $B_0 \sim 0.1$ T. Furthermore, the readout of a single donor spin based upon spin-to-charge conversion[4] requires that the Zeeman energy $h\gamma_e B_0$ far exceed the thermal energy $k_B T$, where k_B is the Boltzmann constant and T is the temperature. As T is typically ~ 100 mK, a minimum $B_0 \sim 1$ T is thus required for high-contrast qubit readout. This value of B_0 sets a challenging requirement for the minimum $J_{c(i)}$ in the chain according to Equation 2. For the example of a 7-electron chain, the minimum $J_{c(i)}/h$ must be > 400 GHz to satisfy $\Delta_c > 10h\gamma_e B_0$.

A. Accuracy of donor placement and chain operation mode

The exchange interactions between donor electrons are extremely sensitive to the position of the donor atoms[34].

Therefore, donor placement accuracy and/or tunability is of paramount importance for quantum devices that exploit the exchange interaction for their functionality. Broadly speaking, there are two methods to controllably incorporate donors within a silicon crystal. The STM method allows near-atomic precision in the placement of the donors[11], but is not entirely deterministic in the number of donors that end up being incorporated at each location, potentially leading to large uncertainty in the actual exchange couplings. Additionally, the low thermal budget in the STM method complicates the growth a high-quality insulating oxide close to the plane that contains the donor, and has so far hindered the ability to electrostatically control STM-incorporated donors through metal gates on the top.

Alternatively, donor atoms can be introduced using the industry-standard ion implantation technique, augmented with methods that allow the counting of each individual ion that enters the substrate[35]. Counted single-ion implantation thus overcomes the uncertainty in donor number, but comes at the price of larger inaccuracy in the final location of each implanted donor[36]. However, recent work has shown impressive placement accuracy with a technique where the ions are first cooled and counted inside an ion trap and then accurately focused onto the silicon chip[37]. For a spin chain, variability in $J_{c(i)}$ can diminish Δ_c past the point where the chain no longer forms a well-defined two-level system. To determine the required positioning accuracy, we must first calculate the exchange interaction between two donors as a function of their separation.

A key point we wish to raise here is that, provided one has the ability to place an electrostatic gate above the donors, the spin chain can be operated in two distinct modes which have significantly different exchange couplings as a function of inter-donor separation. The first mode is in the absence of an electric field, where the chain electrons are confined to their respective donor nuclei, as they are in bulk silicon. We will refer to this operating regime as the 'bulk-like mode,' as illustrated in Figure 2(a). The second mode of operation is where a metallic gate located above the chain donors is used to pull the electrons to the Si-SiO$_2$ interface[38]. For a range of donor depths, 5-20 nm, this 'chain gate' can create a vertical electric field sufficient to ionize the donors, while the electrons are still laterally confined by the Coulomb potential of their respective nuclei[39]. We will refer to this operating regime as the 'interface mode,' as illustrated in Figure 2(b). The calculation of the exchange coupling as a function of inter-donor separation for the two operating modes is given in Appendix A.

On that basis, we proceed to calculate the likelihood that a donor chain fails to satisfy the criterion in Equation 2, typically because enough of the exchange couplings in the chain, $J_{c(i)}$, have become too weak. We perform a Monte Carlo analysis considering chains with $N = 3$, 5 and 7, with targeted inter-donor separation μ_d. For simplicity, we restrict our analysis to donors placed
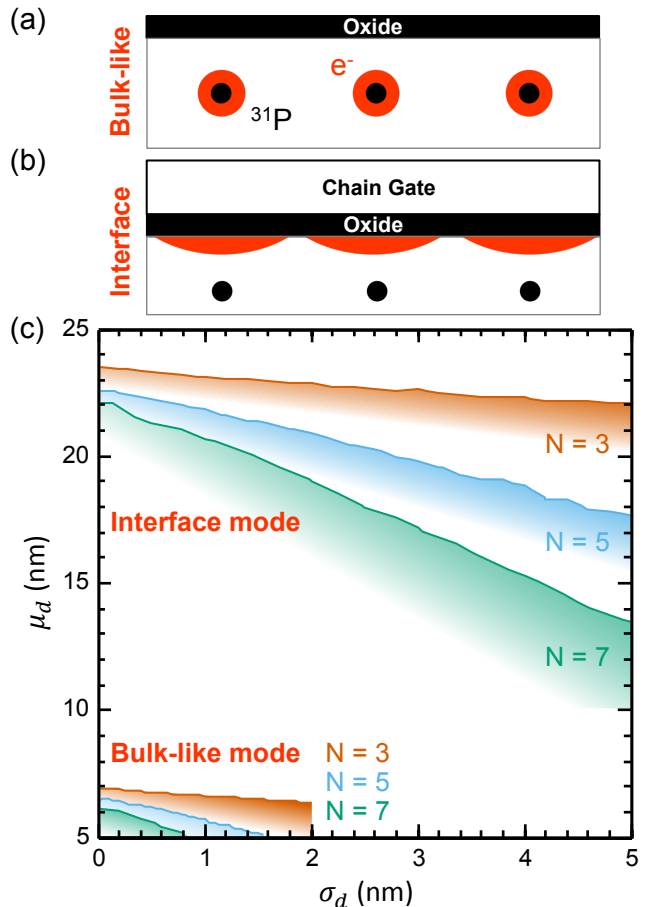

FIG. 2. (Color online) (a)-(b) Schematics of electron orbital wavefunctions in a three-donor chain operated in the (a) bulk-like and (b) interface modes. The electrons and ^{31}P nuclei are represented in red and black, respectively. (c) Targeted inter-donor separation μ_d to obtain at least 90% yield, as a function of donor placement error σ_d. Chains are simulated for the bulk-like and interface modes for $N = 3$, 5 and 7, with $B_0 = 1$ T. The donors in the chain are assumed to be placed along the [100] crystallographic axis. Pulling electrons to the Si-SiO$_2$ interface with a chain gate increases the robustness of the chain to donor placement inaccuracies.

along the [100] crystallographic axis, where the exchange coupling follows a smooth exponential decay with donor separation[40]. An error is introduced in the donor positions along the direction of the chain, following a normal distribution with standard deviation σ_d. For each chain simulated, we numerically solve the N-electron Hamiltonian H_{c_e} to determine the energy separation Δ_c, which determines whether or not the chain functions as an extended qubit. We define the 'yield' as the proportion of chains that satisfy the condition $\Delta_c > 10h\gamma_e B_0$ after performing 10,000 simulations.

Figure 2 shows the 90% yield contours for both the bulk-like and interface modes as a function of μ_d and σ_d when $B_0 = 1$ T, for $N = 3$, 5 and 7. Some clear trends

can be identified. The values of μ_d at $\sigma_d = 0$ nm for the six curves in the plot are different. Comparing chains operated in the same mode, we see that the initial μ_d decreases with increasing N, as Δ_c is inversely proportional to N (Equation 3). The allowed separation for the interface mode is also much greater than that of the bulk-like mode. This is due to the greater lateral spread of the orbital wavefunction of the interface electron compared to the donor-bound electron[38,39], which leads to a significant enhancement in the exchange couplings $J_{c(i)}$ (refer to Figure 10 in Appendix A). As σ_d increases, μ_d needs to be reduced to ensure that all the intra-chain exchange couplings are sufficiently large to satisfy the condition in Equation 2. The slope is steeper for chains with a greater number of donors as, for a given σ_d, there is a greater chance of two adjacent donors having too weak an exchange coupling.

Figure 2 can be used to determine the chain length achievable given the donor positioning uncertainty for the fabrication process used. For example, with $\sigma_d = 2$ nm, a chain with 3 donors operated in the bulk-like mode is limited to $\mu_d \approx 6.5$ nm, yielding a chain length of only 13 nm. In contrast, much longer chains can be realized when operated in the interface mode. The same uncertainty of 2 nm allows for chains with 3, 5 and 7 donors to have total lengths of ~ 45 nm, ~ 85 nm and ~ 115 nm, respectively. We note that the fabrication overhead to implement an interface-mode chain is minimal, since it only requires one global gate above the entire chain. An equivalent 'interface mode' spin chain could be obtained by fabricating a line of electrostatically-defined quantum dots[10,41], but it would come at the cost of fabricating at least one or two individual gates per dot.

In the above calculations, we only considered uncertainty in donor placement along the crystallographic [100] axis. A more general treatment with positioning errors in all directions would be desirable, but is computationally impractical. In the bulk-like mode, misalignments of the donor position away from the [100] axis can severely modify $J_{c(i)}$. This is due to interference between the six $(k_{\pm x}, k_{\pm y}, k_{\pm z})$ valley components of the donor electron wavefunctions in silicon[34]. On the other hand, the electron wavefunctions in the interface mode are composed of only the k_{+z} and k_{-z} valleys[42], thus removing the valley interference for donors confined to the plane perpendicular to the [001] direction. However, valley interference can still modulate the exchange coupling in the presence of step edges at the Si-SiO$_2$ interface. Moreover, when the donors are implanted at different depths, the lateral size of the interface electron wave-functions would vary within the chain, leading to a variability of $J_{c(i)}$[39].

Overall, we consider the interface mode to be the preferred mode operation for a spin chain, due to its superior robustness against donor placement inaccuracy, and the ability to build much longer chains with the same donor number as compared to the bulk mode.

B. Source and Target Donor Qubits

We now include the source and target donor qubits, with their electron spins exchange-coupled to either end of the chain by $J_{s-c(1)}$ and $J_{t-c(N)}$, respectively. Provided $J_{s-c(1)}$ and $J_{t-c(N)} \ll J_c$, the effective exchange coupling between the source (or target) and chain qubits is given by $J_s \approx J_{s-c(1)}/\sqrt{N}$ (or $J_t \approx J_{t-c(N)}/\sqrt{N}$)[24]. Given realistic values of J_c/h of order 100 GHz, the maximum value of J_s/h and J_t/h would be ~ 10 GHz. The source, chain and target electron qubits can then be mapped on to the following Hamiltonian.

$$
\begin{aligned}
H_{s-c-t} = {} & \epsilon_s \frac{\sigma_{z,s}}{2} + \epsilon_c \frac{\sigma_{z,c}}{2} + \epsilon_t \frac{\sigma_{z,t}}{2} + \\
& J_s \frac{\boldsymbol{\sigma}_s}{2} \cdot \frac{\boldsymbol{\sigma}_c}{2} + J_t \frac{\boldsymbol{\sigma}_c}{2} \cdot \frac{\boldsymbol{\sigma}_t}{2},
\end{aligned}
\tag{4}
$$

where $\boldsymbol{\sigma}_i$ is the Pauli operator with z component $\sigma_{z,i}$. ϵ_i is the energy splitting between the qubit states, where the subscript i denotes the source, chain or target.

We assume that the source and target donors are operated in the bulk-like mode, where the electron and nuclear spins are coupled by the hyperfine interaction A, and that $h\gamma_e B_0 \gg A$ to ensure that the electron-nuclear eigenstates of source and target qubits are disentangled. In this regime, the hyperfine interaction simply modifies the electron qubit splitting by an amount dependent on the nuclear spin state. The latter is known to remain unchanged for several minutes[6] unless forcibly modified by the application of radio-frequency excitations. The source and target qubit splitting, ϵ_s and ϵ_t, are equal to $h\gamma_e B_0 + A/2$ or $h\gamma_e B_0 - A/2$ when the nucleus is in the $|\Uparrow\rangle$ state or $|\Downarrow\rangle$ state, respectively. In the analysis below, we set $\epsilon_s = \epsilon_t$, which can be realized by preparing the nuclear spins of the source and target donors in the same state, and tuning their hyperfine couplings with local electrostatic gates[43] until they acquire identical values.

We address the effect of the nuclear spins on a chain operated in the bulk-like mode in Appendix B. For a chain in the interface mode, however, the hyperfine coupling between the electron and nuclear spins is zero, since the electron wavefunctions do not overlap with those of the nuclei. Therefore, the energy separation ϵ_c between the $|\uparrow_c\rangle$ and $|\downarrow_c\rangle$ chain qubit states is simply equal to $h\gamma_e B_0$.

We define the energy detuning between the source and chain qubits as $\Delta B_z = |\epsilon_s - \epsilon_c|$. In the case of an interface-mode chain, $\Delta B_z = A/2$ regardless of the source qubit nuclear state. We use the notation ΔB_z to highlight that this detuning coincides with the energy difference between the $|\uparrow_s\downarrow_c\rangle$ and $|\downarrow_s\uparrow_c\rangle$ source-chain states, and has the same physical origin as the energy difference between the $|\uparrow\downarrow\rangle, |\downarrow\uparrow\rangle$ states in a singlet-triplet qubit. Here, however, ΔB_z does not depend on the polarization of a large bath of nuclear spins, as would be the case in a double quantum dot system, but simply arises from the fact that one qubit (the source or target) is coupled
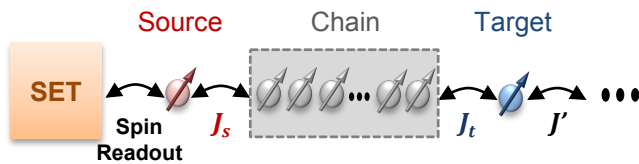
FIG. 3. (Color online) Schematic of the system used for transport. A source donor is exchange-coupled to a donor chain, which is in turn coupled to a target donor. The target donor is then linked to the remainder of the quantum processor. A single-electron transistor (SET) tunnel-coupled to the source donor serves to initialize and measure the state of the source electron spin qubit.

to a single nuclear spin, while the other (the chain) is not. Indeed, recent experiments have shown the potential of this type of donor-dot hybrid systems to realize singlet-triplet qubits with robust values of ΔB_z[44,45].

II. CALIBRATION OF THE SYSTEM

Spin transport across the chain requires control over the exchange couplings J_s and J_t, as will be described in Section III. This control may come from tuning the tunnel barriers between the donor electrons directly[46], or detuning their respective electrochemical potentials[47], with gate electrodes. It is however extremely unlikely, even with atomically precise donor placement, that the magnitude of exchange couplings will match the values targeted during fabrication. Therefore, it will be necessary to first calibrate J_s and J_t to the voltages of the respective gate-electrodes designed to tune them (exchange-gates). For spin transport, the key quantities to record are the minimum and maximum values of the exchange couplings that can be achieved. In addition, it is also important to measure ϵ_i for each qubit, as it can vary due to magnetic field inhomogeneities and DC Stark shifts of the electron g-factor[48] and donor hyperfine interaction[43,49].

Before providing a calibration protocol, we first introduce the way in which a spin chain might be incorporated into a quantum processor architecture, such as the one presented in Reference 50. A source donor at the edge of the quantum processor is tunnel-coupled to a single-electron transistor (SET) for initialization and readout of its electron and nuclear spins[4,6,51], as illustrated in Figure 3. This donor is then exchange coupled to a donor chain, which is in turn coupled to a target donor. The target donor is linked to the remaining entities of the processor. Due to layout constraints, it may not be possible to fabricate an SET for every donor qubit in the processor for initialization and readout. We have thus developed a protocol to calibrate and initialize the qubits, regardless of their distance from the edge of the processor.

Our calibration protocol relies on the assumption that any qubit or a pair of qubits can be effectively isolated

from the remainder of the processor. For example, when the source donor is being calibrated, one must ensure that the chain does not alter its dynamics. Similarly, when J_s is being calibrated, the target should not alter the dynamics of the source-chain system. This isolation may be achieved in two steps. We present these steps using the example of isolating the source donor. First, J_s should be minimized by pulsing its exchange-gate appropriately. However, it would be unrealistic to assume that $J_s = 0$. The source qubit, therefore, is not completely separated from the dynamics of the chain. The second step utilizes J_t to minimize the effect of a non-zero J_s. Maximizing J_t, i.e. strongly coupling the chain and target qubits, has the effect of isolating the dynamics of the source qubit. This is because the eigenstates of the system will then approximately be the tensor products of the uncoupled source qubit states with the singlet-triplet states of the chain and target, similar to the case where $J_s = 0$. The required ratio of J_t to J_s for this isolation will be quantified in Section III B 3. We assume that the above steps are sufficient to isolate any qubit (or pair of qubits) in the processor that is being calibrated.

We begin by determining ϵ_s of the isolated source donor. The spin state of the source electron is measured and initialized using spin-dependent tunneling to the SET[4]. ϵ_s can then be extracted using the electron spin resonance (ESR) technique outlined in Reference 5.

The next step is to calibrate J_s with its exchange-gate (J_s-gate) voltage. For this, the chain is first isolated from the target, by minimizing J_t and maximizing J' (Figure 3). Then, the ESR spectrum of the source qubit is measured while varying the J_s-gate voltages. The exchange coupling J_s modifies the source resonance frequencies and provides a unique 'fingerprint' that can be compared to the theoretically calculated ESR spectrum described below, resulting in an accurate map of J_s as a function of J_s-gate voltage.

Figure 4(a) shows the ESR spectrum of the source electron as a function of J_s, calculated by solving for the eigenstates of the Hamiltonian:

$$H_{s-c(\text{interface})} = h\gamma_e B_0 \left(\frac{\sigma_{z,s}}{2} + \frac{\sigma_{z,c}}{2} \right) - h\gamma_n B_0 \frac{^{\text{nuc}}\sigma_{z,s}}{2} + A\frac{\boldsymbol{\sigma}_s}{2} \cdot \frac{^{\text{nuc}}\boldsymbol{\sigma}_s}{2} + J_s \frac{\boldsymbol{\sigma}_s}{2} \cdot \frac{\boldsymbol{\sigma}_c}{2},$$

$$(5)$$

where $^{\text{nuc}}\boldsymbol{\sigma}_s$ is the Pauli operator for the source nucleus with z-component $^{\text{nuc}}\sigma_{z,s}$, and $\gamma_n \approx 17.2$ MHz/T is the nuclear gyromagnetic ratio for the ^{31}P donor. To obtain a model ESR spectrum that would match the experiment described, for each value of J_s, we weigh all possible transitions between the eigenstates of $H_{s-c(\text{interface})}$ with the product of the transition probability and spin readout contrast of the source qubit [52]. This corresponds to the readout signal available in the experiment, which is the spin of the source electron. The resonance frequencies obtained in the experiment at a particular voltage on the
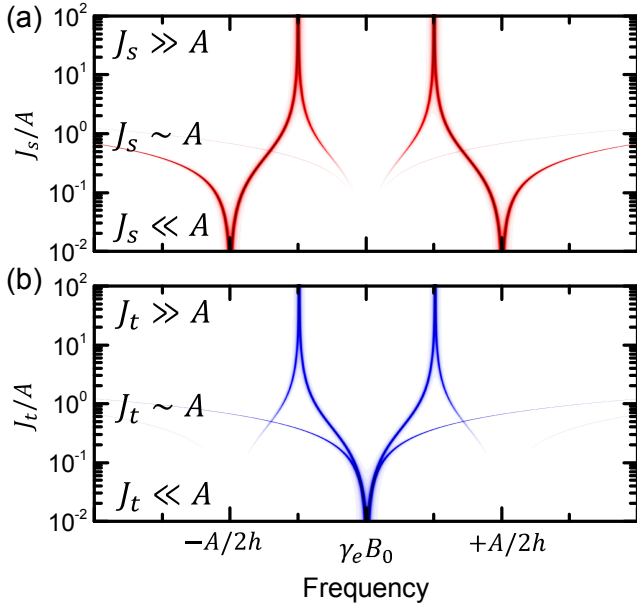
FIG. 4. (Color online) ESR spectra of a donor electron coupled to a chain qubit, operated in the interface mode. The spectra are shown for the cases where measurement of only (a) the donor electron or (b) the chain qubit is possible. (a) and (b) are used to calibrate J_s and J_t, respectively.

J_s-gate corresponds to a horizontal slice in the plot.

We now briefly describe the physics in Figure 4(a). For $J_s \ll A/2$, the ESR spectrum is that of the isolated source donor, where the two hyperfine-split peaks[5] correspond to the two possible frequencies of $\epsilon_s/h = \gamma_e B_0 \pm A/2h$. As J_s is increased with its exchange-gate, each of the peaks split into two branches corresponding to the two possible states of the chain qubit, $|\uparrow_c\rangle$ and $|\downarrow_c\rangle$. This splitting is equal to J_s/h, allowing its magnitude to be directly obtained in the low J_s ($< A/2$) regime. As J_s is increased further ($> \Delta B_z = A/2$), the eigenstates of the coupled source and chain qubits evolve towards the spin-singlet $|S\rangle$ and the triplet states, $|T_0\rangle$, $|T_+\rangle$ and $|T_-\rangle$. The branches that involve the $|S\rangle$-like state fade away as their transition probabilities tend to zero. In contrast, the branches that involve the $|T_0\rangle$-like state tend towards a frequency that is the average of the isolated source and chain qubit frequencies, i.e. $(\epsilon_s + \epsilon_c)/2h$. This is equal to $\gamma_e B_0 \pm A/4h$ as shown at the top of Figure 4(a), depending on the spin of the source nucleus.

While the low ($< A/2$) values of J_s can be extracted directly from the ESR spectrum, a different technique is required to estimate them when $J_s > A/2$. In this regime, J_s can be measured using a SWAP-style experiment, as detailed in the sequence below.

i. Initialize the source-chain system in anti-parallel states while J_s is minimized. For this, the chain qubit needs to be read out using a conditional-rotation (CROT) on the source qubit[52]: with the source initialized in the $|\downarrow\rangle$ state and J_s pulsed to $\ll A/2$, an ESR π-pulse is applied at the frequency where the source qubit flips only if the chain is in the $|\downarrow\rangle$ state. If the source has not flipped, then the chain has been determined to be in the $|\uparrow\rangle$ state. The source qubit should then be initialized in the opposite state to the chain qubit.

ii. Measure the frequency of exchange oscillations. With the system initialized in anti-parallel states, J_s is pulsed high ($> A/2$) for a time τ, and then minimized thereafter. The source qubit is then readout to see if it has flipped. This is repeated several times to obtain a flip-probability. The flip-probability can be plotted as a function of τ, and will display exchange oscillations at frequency J_s.

The chain qubit splitting ϵ_c is calibrated by measuring its ESR spectrum, using the fact that its spin state can be read out via CROT of the source qubit in the $J_s \ll A/2$ regime. Similarly, access to the spin state of the chain qubit allows the calibration of J_t to its associated exchange-gate with the same method used to calibrate J_s. Figure 4(b) shows the ESR spectrum of the chain qubit as a function of J_t. This spectrum is obtained by solving the Hamiltonian in Equation 5, but where the source is replaced by the target and the readout contrast is based on the chain qubit instead. In the low J_t regime, the ESR spectrum is that of the isolated chain qubit, whereas the spectra of Figure 4(a) and (b) converge in the high J_s or J_t regime.

The above techniques can thus be used recursively to (i) initialize and readout any qubit, (ii) measure ϵ_i of each qubit, and (iii) calibrate the exchange interaction to its associated gate for any pair of qubits in the processor. As we shall explain below, a particularly important parameter for the operation of the chain is the maximum exchange coupling achievable between chain and qubits, $J_{\max}$.

Note that our analysis in this section focused on a donor chain operated in the interface mode. For completeness, we also present the calibration protocol and ESR spectra for the case where the chain is operated in the bulk-like mode in Appendix C.

III. SPIN TRANSPORT

In this section, we analyze the transport of a source qubit to the target qubit via the chain. For our analysis, we define the transport fidelity as:

$$F = |\langle \Psi_f | \Psi_r \rangle|^2, \tag{6}$$

where $|\Psi_r\rangle$ is the required final state of the source-chain-target system and $|\Psi_f\rangle$ is the actual final state of the system after transport.
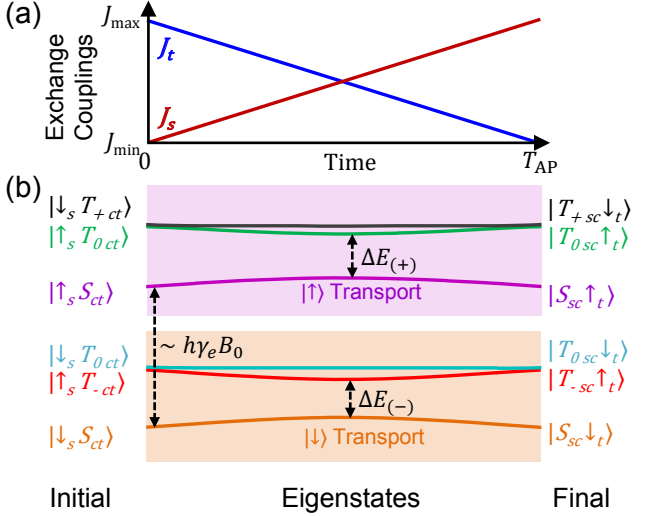
FIG. 5. (Color online) (a) Pulsing scheme for the adiabatic spin transport protocol. (b) Sketch of the time evolution of the eigenenergies (y-axis not to scale). The approximate eigenstates are labeled at the start and end of the protocol. The $|\uparrow\rangle$ and $|\downarrow\rangle$ states are transported via the two labeled adiabatic passages. They belong to two independent blocks of the Hamiltonian as grouped by the shaded boxes.

An intuitive method for transporting the source qubit to the target is via sequential SWAP operations[24], where the spin state is first transferred to the chain and then to the target. A SWAP operation is achieved by pulsing the exchange coupling J (i.e. J_s or J_t) to a value much larger than ΔB_z (Reference 52), for a time T_{SWAP}, such that $\int_0^{T_{\mathrm{SWAP}}} [J(t)/h]\, dt = 0.5$. For example, T_{SWAP} needs to be 50 ps for $J(t)/h = 10$ GHz. Defining $\bar{J}$ as the mean exchange coupling during a SWAP operation, the transport fidelity is given by

$$F_{\mathrm{SWAP}} \approx \sin^4\left(\pi T_{\mathrm{SWAP}}\bar{J}/h\right). \tag{7}$$

While the SWAP operation is fast, F_{SWAP} is sensitive to noise in J and timing imperfections. Equation 7 shows that an accuracy of $\bar{J}T_{\mathrm{SWAP}}$ to within 2% is required to obtain $F_{\mathrm{SWAP}} > 99\%$. In the example where $J(t)/h = 10$ GHz and $T_{\mathrm{SWAP}} = 50$ ps, this translates to a requirement of pulses with picosecond precision. To circumvent this timing constraint, an adiabatic transport protocol robust to pulsing errors was proposed in Reference 31.

An adiabatic process is one in which the instantaneous eigenstates of the system are modified at a rate much slower than the energy separations between them. The Hamiltonian H_{s-c-t} in Equation 4 is block diagonal, as explained in Reference 31. We analyze the adiabatic transport process by starting with $J_s = 0$ and $J_t = J_{\max}$ at $t = 0$. At this point, the eigenstates are the uncoupled source spin state and the chain-target singlet and triplet states, as labeled on the left side of Figure 5(b).
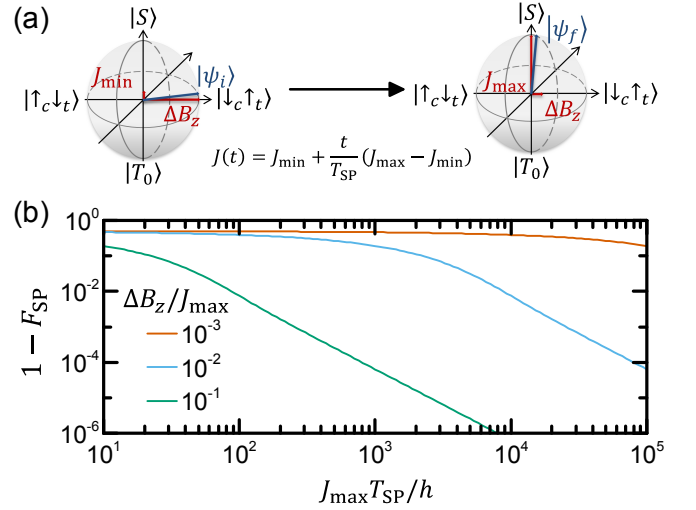

FIG. 6. (Color online) (a) Protocol for initializing the chain and target qubits into the near-singlet $|\varphi_{S_{ct}}\rangle$ state of chain and target qubits. (b) Initialization error as a function of the product of T_{SP} and $J_{\max}$, for three values of $\Delta B_z/J_{\max}$. The fidelities are approximately given by Equation 8.

The source holds the qubit state to be transported, $|\psi_s\rangle$, and the chain and target qubits must be initialized in the singlet state $|S_{ct}\rangle$ (see Section III A below). The system is thus in a superposition of the $|\uparrow_s\, S_{ct}\rangle$ and $|\downarrow_s\, S_{ct}\rangle$ eigenstates, which belong to two independent three-state blocks in the Hamiltonian. These blocks are grouped by the shaded boxes in Figure 5(b). Note here that we have omitted the $|\uparrow_s\, T_{+ct}\rangle$ and $|\downarrow_s\, T_{-ct}\rangle$ states in the figure as they are in separate blocks of H_{s-c-t} and do not play a role in transport.

Once initialized, the transport protocol is completed by ramping J_s towards $J_{\max}$ and J_t towards 0 over a time T_{AP}, as shown in Figure 5(a). The evolution of the eigenenergies as a function of time is shown in Figure 5(b), revealing that the $|\uparrow_s\rangle$ and $|\downarrow_s\rangle$ components follow two independent adiabatic passages. The two passages are identical if $\Delta B_z = 0$. At the end of the protocol, the eigenstates are essentially reflections of the $t = 0$ states. The source qubit is transported to the target, and the prepared singlet is reflected on to the source and chain qubits.

Prior to estimating the fidelity of the adiabatic protocol (Section III B), we will outline a method to initialize the target and chain for transport.

A. Singlet Initialization for Adiabatic Transport

Recall from Section I that the required magnetic field is ~ 1 T and the maximum value of J_s/h and J_t/h is ~ 10 GHz. Therefore, the ground-state of the chain-target system when J_t is at its maximum is the $|T_{-ct}\rangle$ state, rather than the singlet $|S_{ct}\rangle$ state. This rules out

several well-established techniques to initialize two qubits in the singlet state that require it to be their ground state[30]. Below we show that we can nevertheless initialize a singlet state by making use of the presence of a finite ΔB_z. The idea is similar to the way in which the $|\uparrow\downarrow\rangle$ or $|\downarrow\uparrow\rangle$ states are initialized in singlet-triplet qubits[30].

We begin with the chain and target qubits in the ground $|T_{-ct}\rangle$ state with minimal J_s and J_t, using the techniques described in Section II. For ease of explanation, we assume that the nuclei of the source and target donors are both initialized in the $|\Downarrow\rangle$ state. ESR is then used to excite the two qubits to $|\psi_i\rangle$ as labeled in Figure 6(a). $|\psi_i\rangle$ is the lower-energy state of the two anti-parallel eigenstates in the low-J regime, and is equal to $|\widetilde{\downarrow_c\uparrow_t}\rangle = \cos(\theta_2)|\downarrow_c\uparrow_t\rangle + \sin(\theta_2)|\uparrow_c\downarrow_t\rangle$, where $\tan(2\theta_2) = J_{\min}/\Delta B_z$. J_t is then increased adiabatically to $J_{\max}(\gg \Delta B_z)$ over a timescale T_{SP} such that the initialized state $|\psi_i\rangle$ evolves to $|\psi_f\rangle$, as shown in Figure 6(a).

Observe that the prepared state $|\psi_f\rangle$ is not exactly equal to the singlet state. ΔB_z modifies the eigenstate of the chain-target system from the exact singlet to a 'near singlet' state, $|\varphi_{S_{ct}}\rangle = \cos(\theta_1)|S_{ct}\rangle - \sin(\theta_1)|T_{0ct}\rangle$, where $\tan(2\theta_1) = \Delta B_z/J_{\max}$. The effect of the discrepancy between the $|\varphi_{S_{ct}}\rangle$ state and the ideal initial state $|S_{ct}\rangle$ on the adiabatic transport protocol will be addressed later in Section III B 2. Here, we only focus on the fidelity with which this initialization protocol prepares the $|\varphi_{S_{ct}}\rangle$ state.

The fidelity F_{SP} is calculated as a function of T_{SP}, the time over which J_t is ramped. F_{SP} is defined as the squared-projection of the final chain-target state onto the required $|\varphi_{S_{ct}}\rangle$ state. Figure 6(b) plots the error $1 - F_{\text{SP}}$ as a function of the product $J_{\max}T_{\text{SP}}/h$ for $\Delta B_z/J_{\max} = 10^{-1}$, 10^{-2} and 10^{-3}. For simplicity we assume $J_{\min} = 0$. Recall that the adiabaticity of an adiabatic protocol is enhanced when the minimum energy separation between the eigenstates and/or the duration of the protocol is increased. Therefore the fidelity improves as T_{SP} is increased, as long as dephasing can be neglected. This is illustrated in Figure 6(b) by considering a fixed $J_{\max}$ and ΔB_z. In addition, the fidelity improves by increasing ΔB_z, since it determines the minimum energy separation between the two eigenstates in this Bloch sphere during the adiabatic protocol. This is also observed in the figure by considering a fixed $J_{\max}$ and T_{SP}. The expression below, derived in Appendix E, is an approximation for F_{SP} in the adiabatic regime:

$$1 - F_{\text{SP}} \approx \frac{1}{4\left(J_{\max}T_{\text{SP}}/\hbar\right)^2}\left(\frac{J_{\max}}{\Delta B_z}\right)^4. \quad (8)$$

Figure 6(b) shows that high initialization fidelities are achievable with this protocol. For example, an initialization error of $< 10^{-4}$ can be obtained for $\Delta B_z/h = 100$ MHz, $J_{\max}/h = 10$ GHz, and $T_{\text{SP}} > 10$ μs. However, we note that the required T_{SP} are several orders of magnitude larger than the timescales for the transport protocol,
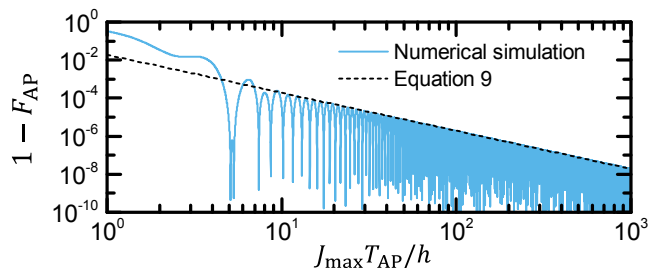

FIG. 7. (Color online) Error of the transport protocol as a function of $J_{\max}T_{\text{AP}}/h$, assuming $\Delta B_z = 0$ and $J_{\min} = 0$. The envelope of the transport error in the adiabatic regime is given by Equation 9 (dashed line). The protocol is highly robust to errors in $J_{\max}$ and T_{AP}.

as will be discussed in the next section. Nonetheless, the initialization protocol need only be performed once, since the prepared state can be reused. This is due to the fact that the transport protocol reflects the $|\varphi_{S_{ct}}\rangle$ state on to the source and chain qubits, as illustrated in Figure 5(b).

B. Adiabatic transport under realistic experimental conditions

We will now investigate the influence of the following experimental parameters on the adiabatic transport protocol: (i) Errors in T_{AP} and/or $J_{\max}$; (ii) ΔB_z between the chain and source/target qubits; (iii) Limited tunability of the exchange couplings; (iv) Noise in the qubit energy splittings ϵ_i; (v) Noise in the exchange couplings J_s and J_t. We define the transport fidelity F_{AP} for transporting a source state $|\psi_s\rangle$ according to Equation 6. Here, the required final state of the system is $|\Psi_r\rangle = |\varphi_{S_{ct}}\rangle \otimes |\psi_s\rangle$.

1. Errors in $J_{\max}$ and T_{AP}

$J_{\max}$ and T_{AP} are the fundamental transport parameters as they determine the degree of adiabaticity of the protocol[31]. To illustrate this, it is instructive to first consider the case where $\Delta B_z = 0$. In this case, the minimum energy separations $\Delta E_{(\pm)}$ between each adiabatic passage and the nearest eigenstate in their blocks are equal to $J_{\max}/2$ [see Figure 5(b)]. To maintain adiabaticity, we require the transport time $T_{\text{AP}} \gg h/\Delta E_{(\pm)}$, and hence the transport fidelity F_{AP} is dependent on the product $J_{\max}T_{\text{AP}}/h$.

Figure 7 shows the transport error, $1 - F_{\text{AP}}$, as a function of $J_{\max}T_{\text{AP}}/h$, obtained from numerical simulations of transporting the $|\psi_s\rangle = (|\uparrow\rangle + |\downarrow\rangle)/\sqrt{2}$ state. We note that fidelities calculated here are independent of the choice of $|\psi_s\rangle$. The resonances indicate points where perfect adiabatic transport is achieved[31]. However, we focus on the envelope to provide a conservative

estimate of fidelities. For large $J_{\max}T_{\mathrm{AP}}/h$, Reference 31 showed that the envelope of the error is proportional to $1/(J_{\max}T_{\mathrm{AP}})^2$. This envelope can also be obtained analytically (Appendix E), and is given by

$$1 - F_{\mathrm{AP}} \approx \frac{3}{3 + (2J_{\max}T_{\mathrm{AP}}/\hbar)^2}. \tag{9}$$

The above equation is also plotted in Figure 7 as the dashed black line. This highlights that the adiabatic protocol is robust to errors in $J_{\max}$ and T_{AP}, and low transport errors of $\sim 10^{-4}$, 10^{-6} and 10^{-8} can be achieved for $J_{\max}T_{\mathrm{AP}}/h \approx 10^1$, 10^2 and 10^3, respectively[31]. Therefore, depending on the targeted fidelity, transport times $T_{\mathrm{AP}} \sim 10 - 100$ ns are required when $J_{\max}/h \sim 1 - 10$ GHz.

Note that the timescales required for T_{AP} are significantly shorter than those required for the singlet initialization protocol time T_{SP}. This is because the transport time is limited by $J_{\max}$, while T_{SP} is limited by $\Delta B_z \ll J_{\max}$.

2. The effect of ΔB_z

The ratio between ΔB_z and $J_{\max}$ also has an important effect on the adiabaticity of the protocol. The energy separations $\Delta E_{(\pm)}$ as a function of ΔB_z are given by:

$$\frac{\Delta E_{(\pm)}}{J_{\max}} = \frac{1 + \sqrt{9 \pm 8\frac{\Delta B_z}{J_{\max}} + 16(\frac{\Delta B_z}{J_{\max}})^2}}{8} \pm \frac{\Delta B_z}{2J_{\max}}. \tag{10}$$

A non-zero ΔB_z decreases $\Delta E_{(-)}$ in Equation 10, and can therefore reduce the adiabaticity of the $|\downarrow_s\rangle$ passage. Figure 8(a) plots the error for transporting a $|\psi_s\rangle = |\downarrow\rangle$ state, as a function of $\Delta B_z/J_{\max}$, for $J_{\max}T_{\mathrm{AP}}/h \approx 10^1$, 10^2 and 10^3. The plot shows that for $\Delta B_z \ll J_{\max}$, the fidelities are limited only by $J_{\max}T_{\mathrm{AP}}/h$, and are given by Equation 9. As ΔB_z increases past a certain point, the reduction of $\Delta E_{(-)}$ causes the $|\downarrow_s\rangle$ passage to lose adiabaticity. From Figure 8(a) we can extract the cut-off value for $\Delta B_z/J_{\max}$, such that ΔB_z does not reduce the transport fidelity, by fitting to the following expression:

$$\left(\frac{\Delta B_z}{J_{\max}}\right)_{\mathrm{cut-off}} \approx \frac{\sqrt{J_{\max}T_{\mathrm{AP}}/h}}{13} \tag{11}$$

Equation 11 shows that, that for $J_{\max}T_{\mathrm{AP}}/h \approx 10^1$, ΔB_z can be as large as $J_{\max}/4$ without affecting the fidelity. In the example of $\Delta B_z/h = 100$ MHz, $J_{\max}/h$ only needs to be as large as ≈ 400 MHz. Even higher values of $\Delta B_z/J_{\max}$ can be tolerated if $J_{\max}T_{\mathrm{AP}}/h$ is increased.

In addition to the adiabaticity, ΔB_z has another effect on the transported state. It breaks the symmetry of the $|\uparrow\rangle$ and $|\downarrow\rangle$ adiabatic passages, since $\Delta E_{(+)} \neq \Delta E_{(-)}$ in
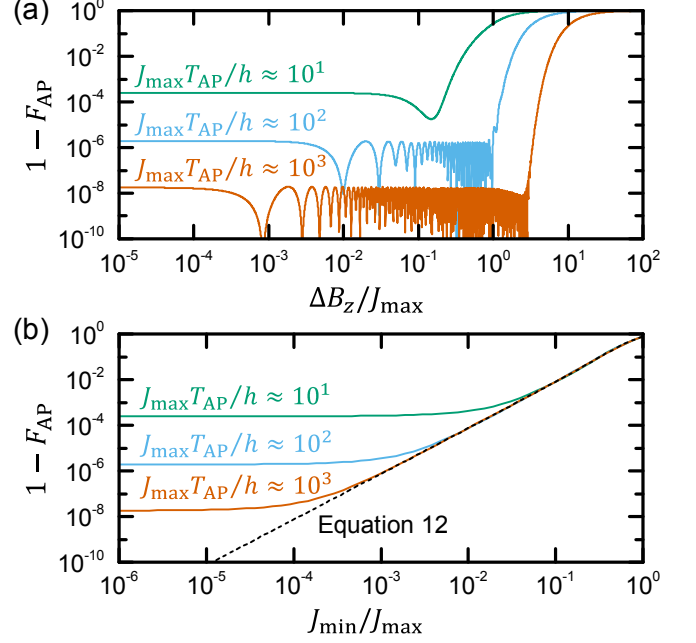

FIG. 8. (Color online) The transport error due to (a) ΔB_z normalized to $J_{\max}$, and (b) limited tunability ($J_{\min}/J_{\max}$) of exchange couplings. These are obtained from numerical simulations of the adiabatic protocol for $J_{\max}T_{\mathrm{AP}}/h \approx 10^1$, 10^2 and 10^3. The cut-off value of $\Delta B_z/J_{\max}$ such that ΔB_z does not affect the transport fidelity is given in Equation 11. The dashed line in (b) is the error due to 'spin-leakage' as described by Equation 12.

Equation 10. The transported state thus acquires a constant phase $\Delta\phi$ with respect to the initial source state. The phase $\Delta\phi$ can be calibrated and corrected for, because it is a function of ΔB_z, $J_{\max}$, (which are determined during the calibration stage) and T_{AP}.

3. Limited tunability of exchange couplings

So far, we have assumed that the exchange coupling can be controlled up to the point of being entirely switched off, $J_{\min} = 0$. A more realistic assumption would allow for a limited dynamic range in the tunability of J, such that some residual exchange coupling remains at all times. For $J_{\min} > 0$, the eigenstates of the system at $t = 0$ are not the simple tensor products of the source qubit state with the coupled states of the chain and target qubits. The transport fidelity then depends on how the system is initialized. If we assume that the system can be initialized such that the source qubit holds the state to be transported $|\psi_s\rangle$ and the chain and target are in the 'near singlet' state $|\varphi_{S_{ct}}\rangle$, the initialized state is not an eigenstate. The source qubit will then undergo partial exchange oscillations ('spin-leakage') with the chain and target, resulting in an error.

To estimate the effect of this spin-leakage, we perform

simulations where we wait for a time $h/J_{\max}$ after the transport protocol, which yields the worst-case fidelity. For simplicity, we assume $\Delta B_z = 0$. Figure 8(b) plots the error of transporting the $|\psi_s\rangle = |\uparrow\rangle$ state as a function of $J_{\min}/J_{\max}$, for $J_{\max}T_{AP}/h \approx 10^1$, 10^2 and 10^3. The fidelities calculated here are independent of the choice of $|\psi_s\rangle$. We observe that the error traces in Figure 8(b) are first limited by Equation 9 ($J_{\max}T_{AP}/h$) and then by spin-leakage for large $J_{\min}/J_{\max}$. An analytical expression for the error due to spin-leakage is derived in Appendix E. This is plotted as the dashed black line in Figure 8(b) and is given by

$$1 - F_{AP} \approx \frac{3}{4} \times (J_{\min}/J_{\max})^2. \qquad (12)$$

The quadratic dependence in Equation 12 allows for low transport errors to be achieved with fairly limited tunability. One and two orders of magnitude of control over the exchange interaction result in errors of 10^{-2} and $\sim 10^{-4}$, respectively. Note that the exchange coupling that needs to be tuned in this system is that between a single donor electron operated in the bulk-like mode (source or target) and an electron at the edge of the chain operated in the interface mode. Estimation of the control on this exchange interaction is left for future work. A recent experiment has demonstrated limited tuning of the exchange coupling in a similar configuration, but the donor in that instance was located almost directly beneath the interface dot[44].

On another note, the spin-leakage error is essentially an estimate of the degree of isolation of the source qubit from the rest of the system. Figure 8(b) illustrates that good isolation can be achieved even with limited tunability of exchange couplings. Recall the technique described in Section II to isolate the source qubit during calibration, where J_t is maximized with respect to J_s. With two orders of magnitude of tunability of exchange couplings, i.e. $J_t/J_s \sim 100$, the source qubit can be treated as being isolated with a fidelity of $\sim 99.99\%$.

4. Noise on the qubit energy splittings ϵ_i

Magnetic and electric noise, arising both within the device and from the external control fields, results in fluctuations in ϵ_s, ϵ_c and ϵ_t. This can lower the fidelity of the transport protocol in two ways. First, the qubit being transported will be subject to dephasing, where an error in $\Delta\phi$ is accumulated. Second, higher-frequency noise can cause fast temporal variations in the instantaneous eigenstates, which can in turn make the transport passages lose adiabaticity.

To estimate the effect of this noise, we simulate the adiabatic transport protocol with independent white Gaussian noise of power spectral density $S_{\delta\epsilon_i}$ added to ϵ_s, ϵ_t and ϵ_c in Equation 4. For each value of $S_{\delta\epsilon_i}$, we perform 1000 simulations and compute the mean fidelity
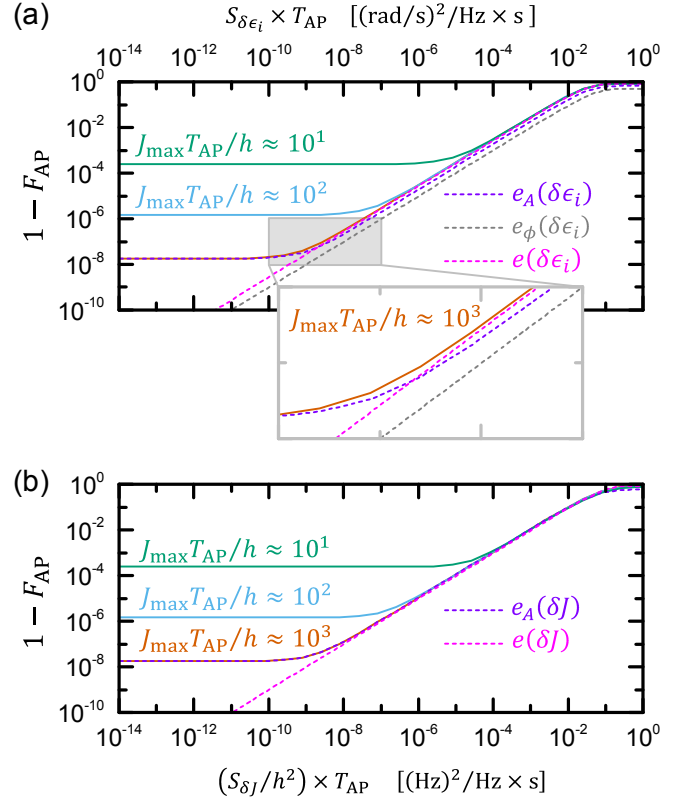

FIG. 9. (Color online) Calculations of error due to noise added to (a) ϵ_s, ϵ_c and ϵ_t and (b) J_s and J_t. The errors are plotted as a function of the product of the power spectral density of the white noise added ($S_{\delta\epsilon_i}$ and $S_{\delta J}$) and T_{AP}. We assume $\Delta B_z/h = 100$ MHz. The solid lines are obtained from numerical simulations of the adiabatic protocol for $J_{\max}T_{AP}/h \approx 10^1$, 10^2 and 10^3. The dashed purple lines correspond to the error due to the loss of adiabaticity for $J_{\max}T_{AP}/h \approx 10^3$. The dashed magenta lines are fits of the total error due to the noise given by Equations 14 and 15. The dashed gray line in panel (a) shows the error due to dephasing.

F_{AP} for transporting the $|\psi_s\rangle = (|\uparrow\rangle + |\downarrow\rangle)/\sqrt{2}$ state, for $J_{\max}T_{AP}/h \approx 10^1$, 10^2 and 10^3, with $\Delta B_z/h = 100$ MHz. We plot these errors as a function of $(S_{\delta\epsilon_i}/h^2) \times T_{AP}$, as the solid lines in Figure 9(a). We express the noise added as $(S_{\delta\epsilon_i}/h^2)$ to yield units of $\mathrm{Hz}^2/\mathrm{Hz}$, which is consistent with the quantities discussed in this paper.

We observe that, in the low-noise regime, the fidelities are limited by the value of $J_{\max}T_{AP}/h$. As the level of noise increases, the fidelities are independent of $J_{\max}$ and instead only depend on the magnitude of the noise and the time that the noise has to act on the system.

The total error is a combination of errors due to dephasing and loss of adiabaticity. To capture the error due to the loss of adiabaticity alone, we perform a separate simulation to obtain the average error $e_A(\delta\epsilon_i)$ of transporting the $|\psi_s\rangle = |\uparrow\rangle$ and $|\psi_s\rangle = |\downarrow\rangle$ states, which are immune to dephasing. $e_A(\delta\epsilon_i)$ is computed for $J_{\max}T_{AP}/h \approx 10^3$ and is plotted as the dashed purple

line in Figure 9(a). We observe that this matches the solid orange line when $\left(S_{\delta\epsilon_i}/h^2\right) \times T_{\mathrm{AP}} < 10^{-10}$. Beyond this value, dephasing also contributes to the total error, separating these two lines, as shown by the inset.

The error due to dephasing of a single qubit, $e_\phi(\delta\epsilon_i)$ in the presence of white noise is given by[53]

$$e_\phi(\delta\epsilon_i) = \frac{1 - e^{-T_{\mathrm{AP}}/T_2}}{2} = \frac{1 - e^{-2\pi^2 S_{\delta\epsilon_i} T_{\mathrm{AP}}/h^2}}{2}, \quad (13)$$

where T_2 is the qubit dephasing time. We plot $e_\phi(\delta\epsilon_i)$ as the dashed gray line in Figure 9(a). Assuming the two sources of error to be independent, the total error is given by $e_\phi(\delta\epsilon_i) + e_A(\delta\epsilon_i) - e_\phi(\delta\epsilon_i)e_A(\delta\epsilon_i)$. This matches the solid orange line remarkably well (result not plotted). In the regime where the transport is limited by noise, we fit the error to an exponential function. This yields the fit, $e(\delta\epsilon_i)$ (plotted as the dashed magenta line in Figure 9(a)), given by

$$e(\delta\epsilon_i) \approx 0.83\left(1 - e^{-34 \times S_{\delta\epsilon_i} T_{\mathrm{AP}}/h^2}\right). \quad (14)$$

Comparing these results to the experiment requires knowledge of the frequency-dependence of the power spectral density of the noise. A recent experiment reports the noise spectrum for a donor electron spin qubit in isotopically enriched ^{28}Si to be of the form $9 \times 10^{11}/\omega^{2.5} + 6$ $(\mathrm{rad/s})^2/\mathrm{Hz}$. The frequency-dependent component is attributed to fluctuations in the external magnetic field B_0[7], which would be homogeneous over the typical transport length-scales (~ 100 nm). This effect of this noise component can therefore be refocused with dynamical decoupling[54]. On the contrary, white noise cannot be refocused. With the reported noise floor of 6 $(\mathrm{rad/s})^2/\mathrm{Hz}$, such that $\left(S_{\delta\epsilon_i}/h^2\right) \approx 0.15$, Equation 14 predicts errors of $\sim 10^{-7}$ with $T_{\mathrm{AP}} \approx 100$ ns.

5. Noise in the qubit-chain couplings J_s and J_t

Electrical noise in a gated nanostructure can modify the exchange interactions J_s and J_t. For $\Delta B_z = 0$, noise in J_s and J_t modifies the $|\uparrow\rangle$ and $|\downarrow\rangle$ adiabatic passages equally, such that the phase error of the transported state is zero. However, $\Delta B_z/h \sim 100$ MHz is always finite for an interface-mode chain, breaking the symmetry of the passages and allowing this noise to potentially feed in to the phase of the transported qubit. Additionally, high frequency noise can potentially reduce the adiabaticity of transport by rapidly modifying the instantaneous eigenstates.

We estimate the transport fidelity as a function of $\left(S_{\delta J}/h^2\right) \times T_{\mathrm{AP}}$, where $S_{\delta J}$ is the power spectral density of white noise added to J_s and J_t. For each value of $S_{\delta J}$, we perform a Monte Carlo analysis of 1000 simulations to quantify the fidelity F_{AP} of transporting the $|\psi_s\rangle = (|\downarrow\rangle + |\uparrow\rangle)/\sqrt{2}$ state with $\Delta B_z/h = 100$ MHz.

These errors are plotted as the solid lines in Figure 9(b), for $J_{\max}T_{\mathrm{AP}}/h \approx 10^1$, 10^2 and 10^3. The trend observed is the same as that of Figure 9(a). Note that solid orange line is hidden by the dashed purple line.

To quantify the loss of adiabaticity, we obtain the average error $e_A(\delta J)$ of transporting the $|\psi_s\rangle = |\uparrow\rangle$ and $|\psi_s\rangle = |\downarrow\rangle$ states, as they are immune to dephasing. $e_A(\delta J)$ for $J_{\max}T_{\mathrm{AP}}/h \approx 10^3$ is plotted as the dashed purple line in Figure 9(b). It aligns almost exactly with the solid orange line for $\left(S_{\delta J}/h^2\right) \times T_{\mathrm{AP}} < 10^{-2}$, indicating that the loss of adiabaticity is the main source of error for noise in J_s and J_t. In the regime where the transport is limited by noise, we fit the error to an exponential function. This yields the fit, $e(\delta J)$ (plotted as the dashed magenta line in Figure 9(b), given by

$$e(\delta J) \approx 0.83\left(1 - e^{-11 S_{\delta J} T_{\mathrm{AP}}/h^2}\right). \quad (15)$$

Experimental values for noise on the exchange coupling between donors are not currently available. In any case, our analysis shows that it is favorable to perform the transport protocol in shorter times T_{AP} and larger $J_{\max}$.

Overall, we find that high-fidelity spin-qubit transport across donor chains may be achieved with the adiabatic protocol. This protocol is inherently robust to errors in the precise magnitudes of exchange couplings and the transport time (Figure 7). The inclusion of ΔB_z in the system is utilized to initialize the system for transport. For $\Delta B_z/h \sim 100$ MHz, we find that a minimum $J_{\max}/h$ of 400 MHz is sufficient to ensure that the fidelity is unaffected by ΔB_z (Figure 8(a)). In the case of limited tunability of the exchange coupling, we have found that two orders of magnitude of control is sufficient for fidelities exceeding 99.99% (Figure 8(b)). The magnitude of magnetic noise as measured in a recent experiment in isotopically-purified silicon still allows for errors $\sim 10^{-7}$ to be achieved (Figure 9(a)). As for the noise in the exchange couplings, although we have calculated the transport fidelities as a function of the noise power spectral density, we do not have compatible experimental measurements for comparison.

IV. SUMMARY AND OUTLOOK

We have provided a comprehensive analysis of the operation of an odd-number donor spin chain for the purpose of transporting a spin qubit state across a quantum processor. A key realization is that, while the donor placement accuracy necessary to operate a spin chain in the bulk-like mode imposes extremely tight constraints on donor placement, a much more reliable fabrication pathway can be found by adopting the interface-mode operation. In that mode, the donor placement accuracy achievable with ion implantation process can allow

the fabrication of functional spin chains with high yield. Moreover, because of the wider extent of the electron wave function at the interface, the qubit state can be moved across distance of order 100 nm using a modest number of donors. Because of the absence of hyperfine coupling between donor nuclear spins and their respective electrons while confined at the Si-SiO$_2$ interface, the system has an inbuilt difference in energy splitting between the source/target qubits and the chain that links them. We have shown how to use this property to initialize the system in a state useful for adiabatic transport of a qubit spin state.

Our analysis of the realistic noise sources that could be present in a spin chain device, based upon the existing knowledge of such noise sources in donor spin qubit devices, indicates that spin transport with high fidelity is in principle possible. Therefore, future work can focus on the design and development of large-scale quantum computer architectures where highly coherent donor spin qubits are linked by spin chains. In that context, the method discussed in Section III B 3 to isolate individual qubits from their neighbors may become more broadly significant, because controlling and removing unwanted interactions between physical qubits is vital to the high-fidelity operation of a quantum computer. For example, a combination of single donors and donor chains could be used to isolate information-carrying spins when they are required to be idle. The adiabatic protocol can then be used within the same system to transport these spins to appropriate locations, where they interact with other qubits to perform quantum logic operations.

Appendix A: Exchange coupling calculation with NEMO-3D

In Section I of the manuscript, we estimated the required dopant placement accuracy to successfully realize a donor chain. Part of this calculation involved a numerical estimate of the exchange coupling J as a function of donor separation. For this, we consider two donors A and B placed in a 3-dimensional space $\mathbf{r}$. We first calculate the single-electron wavefunctions $\Psi_A(\mathbf{r})$ and $\Psi_B(\mathbf{r})$ independently for the two donors using NEMO-3D – an atomistic tight-binding simulation package[55,56]. To estimate

J between the two electrons, we use the Heitler-London formula:[57–59]

$$J = \frac{2}{1 - |S_0|^4}\{|S_0|^2 J_0 - K_0\}, \qquad (A1a)$$

$$S_0 = \int_{\mathbf{r}} \Psi_A(\mathbf{r})^* \Psi_B(\mathbf{r}) \ d\mathbf{r} \qquad (A1b)$$

$$J_0 = \int_{\mathbf{r_1}} \int_{\mathbf{r_2}} \Psi_A(\mathbf{r_1})^* \Psi_A(\mathbf{r_1}) \frac{q^2}{4\pi\epsilon_{\mathrm{Si}}|\mathbf{r_1} - \mathbf{r_2}|}$$
$$\Psi_B^*(\mathbf{r_2})\Psi_B(\mathbf{r_2}) \ d\mathbf{r_2} d\mathbf{r_1}, \qquad (A1c)$$

$$K_0 = \int_{\mathbf{r_1}} \int_{\mathbf{r_2}} \Psi_A(\mathbf{r_1})^* \Psi_B(\mathbf{r_1}) \frac{q^2}{4\pi\epsilon_{\mathrm{Si}}|\mathbf{r_1} - \mathbf{r_2}|}$$
$$\Psi_B^*(\mathbf{r_2})\Psi_A(\mathbf{r_2}) \ d\mathbf{r_2} d\mathbf{r_1}, \qquad (A1d)$$

where J_0 and K_0 are commonly referred to as the exchange and Coulomb integrals, respectively. q is the charge of the electron, and ϵ_{Si} is the dielectric constant of silicon. Note that the wavefunctions $\Psi_A(\mathbf{r})$ and $\Psi_B(\mathbf{r})$ in this method are computed independently of each other. This is reasonable provided the separation between the donors is several times the Bohr radii.

Figure 10 plots J as a function of donor separation R, assuming the donors to be placed along the [100] plane at a depth 7.1 nm below a Si-SiO$_2$ interface. Here, we focus on the regime where 10 GHz $< J/h <$ 1 THz, and consider the two operating modes: (i) the bulk-like mode where the electrons are bound to their respective donors, and (ii) the interface mode where the electrons are pulled towards the Si-SiO$_2$ interface with a vertical electric field $E_z = 30$ MV/m. As the donor electrons are pulled to the interface in the interface mode, their wavefunctions expand in the lateral direction (illustrated in the insets of Figure 10), causing J to be enhanced by many orders of magnitude. The interface-mode therefore allows the donors to be separated further apart, while maintaining large exchange couplings within the chain. The dependence of J on donor separation R in Figure 10 can be fitted to an exponential function given by

$$J = J_\lambda e^{-R/R_\lambda} \qquad (A2)$$

In the bulk-like mode, $J_\lambda/h = 119.12$ THz and $R_\lambda = 1.17$ nm. In the interface mode, $J_\lambda/h = 2.34$ PHz and $R_\lambda = 2.64$ nm.

Appendix B: Donor chain operated in the bulk-like mode

The nuclear spins of the chain donors do not influence the qubit transport when the chain is operated in the
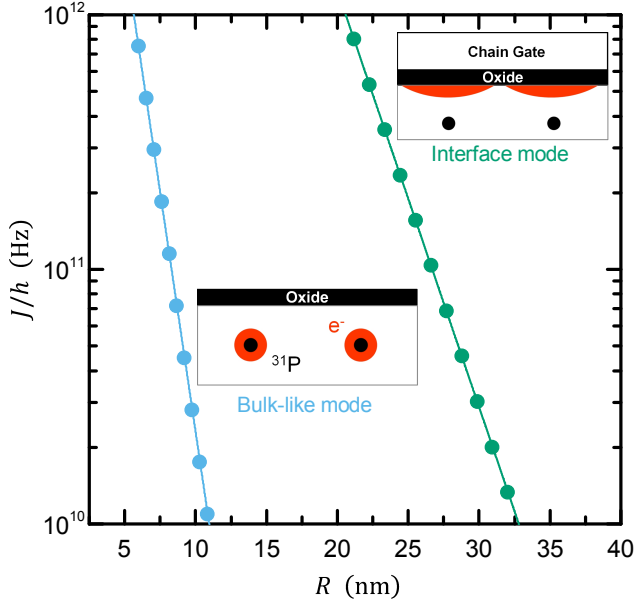
FIG. 10. (Color online) Tight-binding calculation of the exchange coupling as a function of donor separation, for the bulk-like (blue) and interface (green) modes of operation modes. Insets: Schematics of the electron orbital wavefunctions for the two operation modes, with the electrons and ^{31}P nuclei represented in red and black, respectively.

interface mode. However, they have an important effect for a chain operated in the bulk-like mode, since they affect the qubit energy splitting ϵ_c in Equation 4. Here we describe the dependence of ϵ_c on the state of the chain nuclei.

The Hamiltonian for a chain consisting of N donors, including nuclear spins, is given by

$$H_c = H_{c_e} - \sum_{i=1}^{N} h\gamma_n B_0 \frac{^{\mathrm{nuc}}\sigma_{z,c(i)}}{2} + \sum_{i=1}^{N} A_{c(i)} \frac{\boldsymbol{\sigma}_{c(i)}}{2} \cdot \frac{^{\mathrm{nuc}}\boldsymbol{\sigma}_{c(i)}}{2}$$
(B1)

where H_{c_e} is given by Equation 1, $^{\mathrm{nuc}}\boldsymbol{\sigma}_{c(i)}$ is the Pauli operator for the ith chain nucleus with z-component $^{\mathrm{nuc}}\sigma_{z,c(i)}$. $A_{c(i)}$ is the hyperfine coupling between the electron and nuclear spins of the ith chain donor. Recall that for a large magnetic field, e.g. $B_0 = 1$ T, the electron and nuclear spin states can be treated separately. The N electrons form the extended qubit described in Section I, provided Equation 2 is satisfied. For each state of the chain qubit, there are therefore 2^N eigenstates for the nuclei. The resulting ESR spectrum of the chain consists of 2^N resonances, where the chain qubit state is flipped conditional on the state of the nuclear system.

For example, we plot the ESR spectrum for the example of a 3-donor spin chain operated in the bulk-like mode with $B_0 = 1$ T in Figure 11(a). The eight ESR transitions reveal the hyperfine shifts in the chain qubit resonance frequency from $\gamma_e B_0 = 28$ GHz. The frequency

shift, which we denote as $\Delta\nu_c$, is a function of the nuclear state and the individual hyperfine couplings.

We can provide an expression for this shift by first determining the eigenstates of the nuclei. The chain nuclei are mutually coupled by an electron-mediated super-exchange coupling, J_n, which is a function of the individual hyperfine couplings $A_{c(i)}$ and the electronic exchange couplings $J_{c(i)}$[1]. For a 3-donor chain with $J_{c(i)}/h = 1$ THz and $A_{c(i)}/h = 100$ MHz, we numerically calculate that J_n/h between the first and third nuclei is ~ 100 kHz. However, in realistic devices, local electric fields and strain can introduce a Stark shift of order a few MHz in the individual hyperfine couplings $A_{c(i)}/h$[43,49], which in turn detune the nuclei from each other by an amount that typically exceeds the magnitude of their mutual couplings. We account for this by introducing variations in the hyperfine couplings of order 1 MHz in Equation B1. The $\sim$MHz detuning dominates over the weak coupling J_n/h, such that the nuclear eigenstates are almost exactly the tensor products of their individual $|\Uparrow\rangle$ and $|\Downarrow\rangle$ states. We can thus calculate $\Delta\nu_c$ to first order using the equation below.

$$\Delta\nu_c = \sum_{i=1}^{N} U(i) A_{c(i)} C_{c(i)}/h,$$
(B2)

where $U(i)$ equals 1 or -1 when the ith nuclear spin is $|\Uparrow\rangle$ or $|\Downarrow\rangle$, respectively. $2C_{c(i)} = \langle\uparrow_c|\sigma_{zc(i)}|\uparrow_c\rangle = -\langle\downarrow_c|\sigma_{zc(i)}|\downarrow_c\rangle$ represents the 'effective contribution' of the ith chain electron to the chain spin-1/2 ground states. With this result, we can map the effect of the nuclei for a chain operated in the bulk-like mode onto a shift in ϵ_c by an amount $h\Delta\nu_c$.

Appendix C: Calibration of the donor chain in the bulk-like mode

In Section II, we assumed that the chain is operated in the interface mode while calibrating the exchange couplings and the individual qubit energy splittings. This was because experimentally realizing a chain operated in the bulk-like mode is extremely challenging compared to realizing one operated in the interface mode. Here, for completeness, we outline the calibration protocols when the chain is operated in the bulk-like mode.

The architecture including the SET, source donor, donor chain and target donors is identical to that described in Section II of the main text. The difference between the interface and bulk-like modes first appears when measuring the exchange coupling J_s between the source and chain qubits. The ESR spectrum of the source electron will not only show contributions from the state of the chain qubit, but also from the state of the chain nuclei. Figure 11(b) shows the ESR spectrum for a source donor coupled to a 3-donor chain, as a function of the exchange coupling $J_{s-c(1)}$ between the source and the first
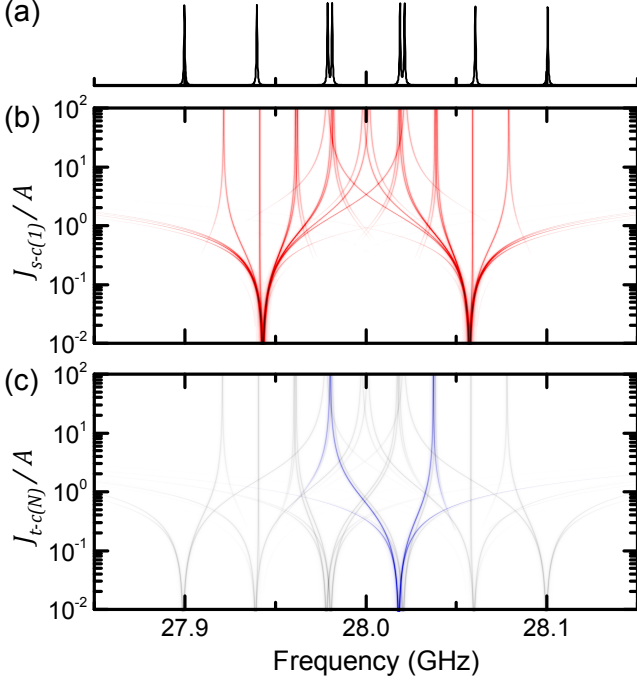
FIG. 11. (Color online (a) Electron spin resonance (ESR) frequencies for a three-donor chain operated in the bulk-like mode, with $B_0 = 1$ T and $J_c/h = 1$ THz. (b) ESR spectrum of a donor coupled to the edge of a $N = 3$ donor chain. (c) ESR spectrum of a $N = 3$ chain qubit coupled to a single donor, i.e. assuming that the chain, not the donor, is being measured.

element of the chain. This spectrum is calculated by numerically solving for the eigenstates of the following Hamiltonian.

$$H_{s-c(\text{bulk})} = H_c + h\gamma_e B_0 \frac{\sigma_{z,s}}{2} - h\gamma_n B_0 \frac{^{\text{nuc}}\sigma_{z,s}}{2} + A_s \frac{\boldsymbol{\sigma}_s}{2} \cdot \frac{^{\text{nuc}}\boldsymbol{\sigma}_s}{2} + J_{s-c(1)} \frac{\boldsymbol{\sigma}_s}{2} \cdot \frac{\boldsymbol{\sigma}_{c(1)}}{2}, \quad \text{(C1)}$$

Note that $J_s \propto J_{s-c(1)}$ as described in Section I. For each value of $J_{s-c(1)}$, we find all allowed transitions between eigenstates of $H_{s-c(\text{bulk})}$ and weigh them with the product of the transition probability and the spin read-out contrast of the source qubit, as done for the interface mode.

Experimentally, to observe all transition frequencies in the ESR spectrum, the chain qubit and nuclei need to be randomized. The NMR frequencies of an N-donor chain are bound between 0 and $\gamma_n B_0 + A/2h$, as will be explained in Appendix D. This makes it possible to randomize the nuclei with non-adiabatic sweeps over the NMR frequencies. Similarly, non-adiabatic sweeps over the ESR frequencies in Figure 11(a) can be used to randomize the chain qubit.

Figure 11(b) shows that in the low $J_{s-c(1)}$ regime, the ESR spectrum of the source electron consists of two tran-

sition frequencies corresponding to the two states of its nuclear spin. As $J_{s-c(1)}$ is increased slightly, these split into a pair of branches due to the coupling to the chain qubit, which can be in either the $|\uparrow_c\rangle$ or $|\downarrow_c\rangle$ state. The branches are split by J_s/h, allowing J_s to be calibrated from the ESR spectrum. For large $J_{s-c(1)}$ ($\gg A$), the branches involving the $|T_0\rangle$-like state tend towards the average of the uncoupled source and chain qubit frequencies, $(\epsilon_s + \epsilon_c)/2h$. This results in 2×2^N possible frequencies, since there are N nuclei in the chain. For $J_s \gg A$, J_s can be calibrated using the SWAP-style experiments outlined in Section II. Once J_s has been calibrated, ϵ_c (and therefore ΔB_z) can be determined by performing ESR on the isolated chain qubit, as explained in Section II.

Figure 11(c) then shows the ESR spectrum of the chain qubit coupled to a target donor, for the purpose of calibrating J_t. In the low J_t regime, the chain qubit has eight possible transition frequencies corresponding to those in Figure 11(a). Highlighted in bright blue are the branches corresponding to a particular nuclear configuration ($|\Downarrow\Downarrow\Uparrow\rangle$) of the chain. This was done to simplify the understanding of the spectrum, as well as to show that J_t can be obtained even if the chain nuclei are not randomized.

Appendix D: NMR frequencies of a donor chain in the bulk-like mode

Recall from Appendix B that the nuclear eigenstates of a realistic donor chain in bulk-like mode would be tensor products of $|\Uparrow\rangle$ and $|\Downarrow\rangle$ states of the chain nuclei. The NMR frequency ν_{ni} for flipping the ith chain nucleus to first order is given by

$$\nu_{ni} = |-\gamma_n B_0 \pm C_{c(i)} A/h|, \quad \text{(D1)}$$

where $C_{c(i)}$ is as defined in Equation B2. The sign is $+$ or $-$ when the chain qubit state is $|\uparrow_c\rangle$ or $|\downarrow_c\rangle$, respectively.

$C_{c(i)}$ takes its maximum value of 0.5 when $N = 1$. Hence the maximum value of ν_{ni} is $(\gamma_n B_0 + A/2h)$ for any N. Thus randomized non-adiabatic NMR frequency sweeps from DC to past this maximum value would be sufficient to randomize the nuclei for a donor chain of any size. Practically, the sweep involves applying a frequency-modulated excitation where the rate of change of frequency is faster than, but comparable to, the expected Rabi frequency of a nuclear spin[60].

Appendix E: Fidelity Calculations

In Sections III A and III B, we quantified the fidelities of the singlet initialization protocol and the adiabatic transport protocol, respectively. Here, we outline the derivations used to obtain Equations 8, 9 and 12.

1. Singlet Initialization Fidelity

The singlet initialization protocol involves initializing the chain-target system in the $|\widetilde{\downarrow_c\uparrow_t}\rangle$ state, as defined in Section III A, and ramping the exchange coupling between the chain and target qubits. The $|\uparrow_c\uparrow_t\rangle$ and $|\downarrow_c\downarrow_t\rangle$ states are not coupled to either the $|\uparrow_c\downarrow_t\rangle$ or $|\downarrow_c\uparrow_t\rangle$ states. Therefore, the dynamics of the protocol can be represented in the S-T_0 Bloch sphere, as illustrated in Figure 6(a). The truncated Hamiltonian in the basis $\{|T_{0ct}\rangle, |S_{ct}\rangle\}$ is given by

$$H_{SP}(t) = J(t)\frac{\sigma_z}{2} + \Delta B_z \frac{\sigma_x}{2}, \quad (E1)$$

where $J(t)$ is the exchange coupling between the chain and target, and is linearly ramped from 0 to J_{max}. The aim is to have the system in the $|\varphi_{S_{ct}}\rangle$ eigenstate at the end of the protocol, as defined in Section III A. Therefore, to quantify the fidelity of the protocol, we translate the Hamiltonian into the adiabatic frame. The translated Hamiltonian $H_{SP}^A(t)$ is obtained by applying the following operation

$$H_{SP}^A(t) = AH_{SP}A^{-1} - i\hbar A\frac{d}{dt}(A^{-1}), \quad (E2)$$

where the row vectors of A are the time-varying eigenvectors of $H_{SP}(t)$.

$$H_{SP}^A(t) = \sqrt{J(t)^2 + (\Delta B_z)^2}\frac{\sigma_z}{2} - \hbar\frac{d\chi_{SP}}{dt}\frac{\sigma_y}{2}, \quad (E3)$$

where $\tan(\chi_{SP}) = \Delta B_z/J(t)$. To gain insight into the energy terms in H_{SP}^A, it is instructive to compare the system in the adiabatic frame onto a spin in a magnetic field (Figure 12). In this picture, the field in the z-direction is the energy separation of the eigenstates of H_{SP}. The field in the y-direction is proportional to the rate of change of the angle of the eigenstate in the Bloch sphere of H_{SP} (the laboratory frame). The eigenvectors of $H_{SP}^A(t)$ are given by

$$|\Phi_{1_{SP}}(t)\rangle = \begin{pmatrix} \cos(\alpha_{SP}) \\ -i\sin(\alpha_{SP}) \end{pmatrix}, \quad (E4a)$$

$$|\Phi_{2_{SP}}(t)\rangle = \begin{pmatrix} \sin(\alpha_{SP}) \\ i\cos(\alpha_{SP}) \end{pmatrix}, \quad (E4b)$$

where $\tan(2\alpha_{SP}) = \hbar\frac{d\chi_{SP}}{dt}/\sqrt{J(t)^2 + \Delta B_z^2}$. The fidelity is determined by the closeness of the state at the end of the protocol to the $+z$-axis in the adiabatic frame, which is equivalent to the eigenstate of H_{SP}.

The dynamics of the system in the adiabatic frame, H_{SP}^A, is shown in Figure 12. Figure 12(a) shows the initial state of the system, which is oriented along z, as we start
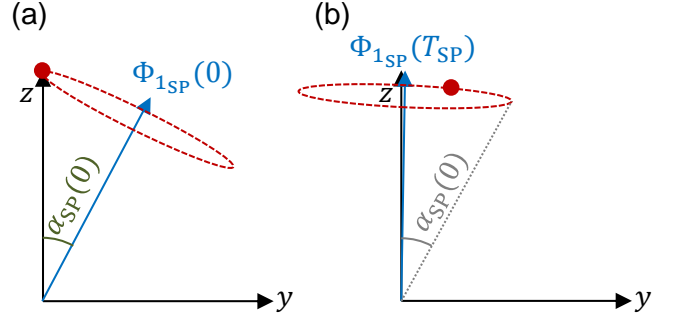

FIG. 12. (Color online) Bloch sphere in the adiabatic frame at the (a) start and (b) end of the singlet initialization protocol. The red dot represents the instantaneous state. The initial state of the system is oriented along the z-axis. In the adiabatic limit, the 'circle of precession' (dashed red circle) around the eigenstate $|\Phi_{1_{SP}}(t)\rangle$ (blue arrow) follows the evolution of $|\Phi_{1_{SP}}(t)\rangle$ and does not change in diameter.

in an eigenstate of H_{SP}. However, the field along y is non-zero at this point, such that the eigenstate $|\Phi_{1_{SP}}(t)\rangle$ is at an angle $\alpha_{SP}(0)$ from the z-axis. If we consider the protocol to be in the adiabatic limit, then the precession frequency of the initial state around the eigenstate $|\Phi_{1_{SP}}(t)\rangle$ is much faster than $d\alpha_{SP}(t)/dt$. Hence, we can picture the precession trajectory of the state to be a circle around $|\Phi_{1_{SP}}(t)\rangle$ (dashed red circle in Figure 12). In the adiabatic limit, the center of this 'circle of precession' follows $|\Phi_{1_{SP}}(t)\rangle$, and therefore the projection of the instantaneous state onto $|\Phi_{1_{SP}}(t)\rangle$ remains constant.

From Equation E4, we see that α_{SP} tends towards zero at $t = T_{SP}$, as also illustrated in Figure 12(b). At the end of the protocol, the circle of precession is centered close to the z-axis, with its diameter set by $\alpha_{SP}(0)$. Therefore, the squared-projection of the eigenstate at $t = 0$ on to the z-axis is an estimate of the fidelity of the protocol, and is given by

$$1 - F_{SP} \approx \sin^2(\alpha_{SP}(0)) = \frac{1}{2}\left(1 - \sqrt{\frac{K}{1+K}}\right), \quad (E5)$$

where $K = (\Delta B_z/J_{max})^4 \times (J_{max}T_{SP}/\hbar)^2$. In the limit where $K \gg 1$, this can be simplified to

$$1 - F_{SP} \approx \frac{1}{4(J_{max}T_{SP}/\hbar)^2}\left(\frac{J_{max}}{\Delta B_z}\right)^4. \quad (E6)$$

2. Adiabatic Transport Fidelity

a. Adiabaticity errors: $J_{\max}T_{\mathrm{AP}}$

Here we outline the method we use to quantify the fidelity of the adiabatic transport protocol. Our strategy will be to truncate the Hamiltonian of the system to the relevant 3×3 block. We then map this onto a 2×2 Hamiltonian and translate it into the adiabatic frame to estimate the fidelity.

We start with the basic Hamiltonian H_{s-c-t} for the source-chain-target system defined in Equation 4. As described by Oh $et\ al.$, H_{s-c-t} is block-diagonal, consisting of four blocks. Only two blocks play a role in adiabatic transport, as described in Section III B, where one transports the $|\downarrow_s\rangle$ component and the other transports the $|\uparrow_s\rangle$ component of the source qubit. When $\Delta B_z = 0$, these two blocks are identical apart from the Zeeman energy. The Zeeman energy can be ignored, as it is simply an identity offset to the diagonal elements of either block. Either adiabatic transport block is defined by the following Hamiltonian.

$$H_{\mathrm{AP}-3}(t) = \frac{1}{4} \begin{pmatrix} J_t - J_s & 2J_s & 0 \\ 2J_s & -J_s - J_t & 2J_t \\ 0 & 2J_t & J_s - J_t \end{pmatrix} \quad (\mathrm{E7})$$

The basis states of $H_{\mathrm{AP}-3}$ are given by $\{|\downarrow_s\uparrow_c\uparrow_t\rangle, |\uparrow_s\downarrow_c\uparrow_t\rangle, |\uparrow_s\uparrow_c\downarrow_t\rangle\}$ for the spin-up block and $\{|\uparrow_s\downarrow_c\downarrow_t\rangle, |\downarrow_s\uparrow_c\downarrow_t\rangle, |\downarrow_s\downarrow_c\uparrow_t\rangle\}$ for the spin-down block. Arbitrarily, we analyze the fidelity for transporting the $|\uparrow_s\rangle$ source state. The eigenvectors of $H_{\mathrm{AP}-3}$ are given by[31]

$$|\Phi_0(t)\rangle = \frac{1}{\sqrt{3}} \begin{pmatrix} 1 \\ 1 \\ 1 \end{pmatrix}, \quad (\mathrm{E8a})$$

$$|\Phi_\pm(t)\rangle = \frac{1}{\sqrt{N_\pm}} \begin{pmatrix} \sin(\zeta) \\ -\cos(\zeta) \pm \sqrt{q} \\ \cos(\zeta) - \sin(\zeta) \mp \sqrt{q} \end{pmatrix}, \quad (\mathrm{E8b})$$

where $\tan(\zeta) = (J_s(t)/J_t(t))$, $q = 1 - \sin(\zeta)\cos(\zeta)$, and $N_\pm = \mp 2(2\cos(\zeta) - \sin(\zeta))\sqrt{q} + 4q$. For adiabatic transport, the system is initialized in the $|\uparrow_s\ S_{ct}\rangle$ state, which is $|\Phi_-(0)\rangle$.

Recall that the eigenenergies of the $|\uparrow\rangle$-transport and $|\downarrow\rangle$-transport blocks are plotted in Figure 5. We see that in each block, two states anti-cross whereas the energy of one state is constant, suggesting that $H_{\mathrm{AP}-3}(t)$ can be truncated to a 2×2 Hamiltonian. For this, we write $H_{\mathrm{AP}-3}$ in the basis of the eigenstates at $t = T_{\mathrm{AP}}/2$, which can be obtained by substituting $J_s = J_t$ into Equation E8. The new basis states are given by

$$|\Phi_0'\rangle = \frac{1}{\sqrt{3}} \begin{pmatrix} 1 \\ 1 \\ 1 \end{pmatrix}, |\Phi_+'\rangle = \frac{1}{\sqrt{2}} \begin{pmatrix} 1 \\ 0 \\ -1 \end{pmatrix}, |\Phi_-'\rangle = \frac{1}{\sqrt{6}} \begin{pmatrix} 1 \\ -2 \\ 1 \end{pmatrix}. \quad (\mathrm{E9})$$

The Hamiltonian $H_{\mathrm{AP}-3}$ in this basis, $\{|\Phi_0'\rangle, |\Phi_+'\rangle, |\Phi_-'\rangle\}$, is

$$H_{\mathrm{AP}-3}'(t) = \frac{1}{4} \begin{pmatrix} J_t + J_s & 0 & 0 \\ 0 & 0 & \sqrt{3}(J_t - J_s) \\ 0 & \sqrt{3}(J_t - J_s) & -2J_s - 2J_t \end{pmatrix}. \quad (\mathrm{E10})$$

As expected, $H_{\mathrm{AP}-3}'(t)$ is block-diagonal. The initialized state of the system is $|\uparrow_s\ S_{ct}\rangle = (1/2)|\Phi_+'\rangle - (\sqrt{3}/2)|\Phi_-'\rangle$. As the initial population of the $|\Phi_0'\rangle$ is zero, we truncate $H_{\mathrm{AP}-3}'(t)$ to the lower 2×2 block, spanned only by $|\Phi_+'\rangle$ and $|\Phi_-'\rangle$. Adding $(J_s + J_t)I_2$, we obtain

$$H_{\mathrm{AP}-2}'(t) = \frac{1}{4} \begin{pmatrix} J_t + J_s & \sqrt{3}(J_t - J_s) \\ \sqrt{3}(J_t - J_s) & -(J_t + J_s) \end{pmatrix}. \quad (\mathrm{E11})$$

Recall that $J_s + J_t = J_{\max}$ and $J_t - J_s = J_{\max}(1 - 2t/T_{\mathrm{AP}})$. We thus complete our mapping onto a spin in a magnetic field, obtaining

$$H_{\mathrm{AP}-2}'(t) = \varepsilon\frac{\sigma_z}{2} + \Delta_{\mathrm{AP}}(t)\frac{\sigma_x}{2}, \quad (\mathrm{E12})$$

where $\varepsilon = J_{\max}/2$ and $\Delta_{\mathrm{AP}}(t) = (\sqrt{3}J_{\max}/2)(1 - 2t/T_{\mathrm{AP}})$. Note that the initialized state, $|\uparrow_s\ S_{ct}\rangle$ is the lower-energy eigenstate of $H_{\mathrm{AP}-2}'(0)$.

With the mapping complete, we then move to calculating the fidelity of the adiabatic protocol. For this, we translate $H_{\mathrm{AP}-2}'(t)$ into the adiabatic frame, by invoking the same operation used in Equation E2. The Hamiltonian in the adiabatic frame $H_{\mathrm{AP}-2}^A(t)$ can be simplified as

$$H_{\mathrm{AP}-2}^A(t) = \sqrt{\varepsilon^2 + \Delta_{\mathrm{AP}}(t)^2}\frac{\sigma_z}{2} - \hbar\frac{d\chi_{\mathrm{AP}}}{dt}\frac{\sigma_y}{2}, \quad (\mathrm{E13})$$

where $\tan(\chi_{\mathrm{AP}}) = \Delta_{\mathrm{AP}}(t)/\varepsilon$. The eigenvectors of $H_{\mathrm{AP}-2}^A(t)$ are given by

$$|\Phi_{1_{\mathrm{AP}}}(t)\rangle = \begin{pmatrix} \cos(\alpha_{\mathrm{AP}}) \\ -i\sin(\alpha_{\mathrm{AP}}) \end{pmatrix}, \quad (\mathrm{E14a})$$

$$|\Phi_{2_{\mathrm{AP}}}(t)\rangle = \begin{pmatrix} \sin(\alpha_{\mathrm{AP}}) \\ i\cos(\alpha_{\mathrm{AP}}) \end{pmatrix}, \quad (\mathrm{E14b})$$

where $\tan(2\alpha_{\mathrm{AP}}) = \hbar\frac{d\chi_{\mathrm{AP}}}{dt}/\sqrt{\varepsilon^2 + \Delta_{\mathrm{AP}}(t)^2}$. We employ the same technique used in Appendix E 1 to estimate

the fidelity of the protocol. We consider the dynamics in the adiabatic frame and assume the adiabatic limit, where the projection of the instantaneous state onto the eigenstate remains constant. The diameter of the 'circle of precession,' again, is determined by the initial eigenstates in the adiabatic frame, which is at an angle $\alpha_{\mathrm{AP}}(0)$ from the z-axis. The eigenstate at the end of the protocol is oriented at an angle $\alpha_{\mathrm{AP}}(T_{\mathrm{AP}})$ from the z-axis. From Equation E14, we see that $\alpha_{\mathrm{AP}}(T_{\mathrm{AP}}) = \alpha_{\mathrm{AP}}(0)$. Therefore, at the end of the protocol, the circle of precession is at exactly the same position as at $t = 0$. Recall that the fidelity of the adiabatic protocol is the projection-squared of the final state onto the z-axis. The 'circle of precession' touches the z axis, and hence we obtain resonances in the transport fidelities as a function of T_{AP} in Figure 7. To obtain the worst case fidelity, however, we use the opposite point on the circle, which has the maximum angular deviation from the z-axis. This yields an expression for the envelope of transport errors given by

$$1 - F_{\mathrm{AP}} \approx \sin^2(2\alpha_{\mathrm{AP}}(0)) = \frac{3}{3 + (2J_{\mathrm{max}}T_{\mathrm{AP}}/\hbar)^2} \quad (E15)$$

Note that this expression perfectly aligns with the numerical simulations in the adiabatic regime ($J_{\mathrm{max}}T_{\mathrm{AP}}/h \gg 1$) in Figure 7.

b. Exchange tunability errors: $J_{\mathrm{min}}/J_{\mathrm{max}}$

Here we derive an expression for the transport fidelity limited by 'spin-leakage,' as defined in Section III B 3. We set $\Delta B_z = 0$ for simplicity, such that the $|\uparrow\rangle$ and $|\downarrow\rangle$ adiabatic passages are equivalent. In Section III B 3, in the example of transporting the $|\uparrow_s\rangle$ state, we have considered the system to be initialized in the $|\uparrow_s\ S_{ct}\rangle$ state. At $t = T_{\mathrm{AP}}$, the system is transported to the $|S_{sc}\ \uparrow_t\rangle$ state, which is not an eigenstate if $J_{\mathrm{min}} \neq 0$. To quantify the error due to the resulting precession, we express $|S_{sc}\ \uparrow_t\rangle$ as a superposition of the eigenstates of $H_{\mathrm{AP}-3}$, given by

$$|S_{sc}\ \uparrow_t\rangle = c_+|\Phi_+(T_{\mathrm{AP}})\rangle + c_-|\Phi_-(T_{\mathrm{AP}})\rangle, \quad (E16)$$

where $c_\pm^2 = \left[\mp\left(2\cos(\zeta_0) - \sin(\zeta_0)\right) + 2\sqrt{q}\right]/4\sqrt{q}$ with $\tan(\zeta_0) = J_{\mathrm{min}}/J_{\mathrm{max}}$. For $J_{\mathrm{min}}/J_{\mathrm{max}} < 1$, $c_- > c_+$. The precession frequency is $\sim J_{\mathrm{max}}/h$. The maximum error is when the state rotates by an angle π around the eigenstate, such that the state of the system becomes $c_+|\Phi_+(T_{\mathrm{AP}})\rangle - c_-|\Phi_-(T_{\mathrm{AP}})\rangle$. This worst-case leads to a fidelity given by $F_{\mathrm{AP}} = |c_+^* c_+ - c_-^* c_-|^2$, which is the projection onto the $|S_{sc}\ \uparrow_t\rangle$ state. This can be simplified to

$$1 - F_{\mathrm{AP}} = \frac{3}{4} \times \frac{(J_{\mathrm{min}}/J_{\mathrm{max}})^2}{(J_{\mathrm{min}}/J_{\mathrm{max}})^2 - (J_{\mathrm{min}}/J_{\mathrm{max}}) + 1}. \quad (E17)$$

In the limit $J_{\mathrm{min}}/J_{\mathrm{max}} \ll 1$, the transport error takes the form

$$1 - F_{\mathrm{AP}} \approx \frac{3}{4} \times (J_{\mathrm{min}}/J_{\mathrm{max}})^2. \quad (E18)$$

[1] B. E. Kane, "A silicon-based nuclear spin quantum computer," *Nature*, vol. 393, pp. 133–137, May 1998.

[2] A. M. Tyryshkin, S. Tojo, J. J. L. Morton, H. Riemann, N. V. Abrosimov, P. Becker, H.-J. Pohl, T. Schenkel, M. L. W. Thewalt, K. M. Itoh, and S. A. Lyon, "Electron spin coherence exceeding seconds in high-purity silicon," *Nature Mater.*, vol. 11, pp. 143–147, Feb 2012.

[3] K. Saeedi, S. Simmons, J. Z. Salvail, P. Dluhy, H. Riemann, N. V. Abrosimov, P. Becker, H.-J. Pohl, J. J. L. Morton, and M. L. W. Thewalt, "Room-Temperature Quantum Bit Storage Exceeding 39 Minutes Using Ionized Donors in Silicon-28," *Science*, vol. 342, pp. 830–833, Nov 2013.

[4] A. Morello, J. Pla, F. Zwanenburg, K. Chan, K. Tan, H. Huebl, M. Möttönen, C. Nugroho, C. Yang, J. van Donkelaar, *et al.*, "Single-shot readout of an electron spin in silicon," *Nature*, vol. 467, pp. 687–691, Oct 2010.

[5] J. J. Pla, K. Y. Tan, J. P. Dehollain, W. H. Lim, J. J. L. Morton, D. N. Jamieson, A. S. Dzurak, and A. Morello, "A single-atom electron spin qubit in silicon," *Nature*, vol. 489, pp. 541–545, Sep 2012.

[6] J. J. Pla, K. Y. Tan, J. P. Dehollain, W. H. Lim, J. J. L. Morton, F. A. Zwanenburg, D. N. Jamieson, A. S. Dzurak, and A. Morello, "High-fidelity readout and control of a nuclear spin qubit in silicon," *Nature*, vol. 496, pp. 334–338, Apr 2013.

[7] J. T. Muhonen, J. P. Dehollain, A. Laucht, F. E. Hudson, R. Kalra, T. Sekiguchi, K. M. Itoh, D. N. Jamieson, J. C. McCallum, A. S. Dzurak, and A. Morello, "Storing quantum information for 30 seconds in a nanoelectronic device," *Nat. Nanotechnol.*, vol. 9, pp. 986–991, Oct 2014.

[8] J. P. Dehollain, J. T. Muhonen, K. Y. Tan, A. Saraiva, D. N. Jamieson, A. S. Dzurak, and A. Morello, "Single-shot readout and relaxation of singlet and triplet states in exchange-coupled ^{31}P electron spins in silicon," *Phys. Rev. Lett.*, vol. 112, p. 236801, Jun 2014.

[9] M. F. Gonzalez-Zalba, A. Saraiva, M. J. Caldern, D. Heiss, B. Koiller, and A. J. Ferguson, "An exchange-coupled donor molecule in silicon," *Nano Lett.*, vol. 14, pp. 5672–5676, Sep 2014.

[10] M. Veldhorst, C. H. Yang, J. C. C. Hwang, W. Huang, J. P.

Dehollain, J. T. Muhonen, S. Simmons, A. Laucht, F. E. Hudson, K. M. Itoh, A. Morello, , and A. S. Dzurak, "A two-qubit logic gate in silicon," *Nature*, vol. 526, pp. 410–14, Oct 2015.

[11] M. Fuechsle, J. A. Miwa, S. Mahapatra, H. Ryu, S. Lee, O. Warschkow, L. C. L. Hollenberg, G. Klimeck, and M. Y. Simmons, "A single-atom transistor," *Nat. Nanotechnol.*, vol. 7, pp. 242–246, Feb 2012.

[12] N. H. Nickerson, Y. Li, and S. C. Benjamin, "Topological quantum computing with a very noisy network and local error rates approaching one percent," *Nat. Commun.*, vol. 4, p. 1756, Apr 2013.

[13] J. M. Taylor, H.-A. Engel, W. Dr, A. Yacoby, C. M. Marcus, P. Zoller, and M. D. Lukin, "Fault-tolerant architecture for quantum computation using electrically controlled semiconductor spins," *Nat. Phys.*, vol. 1, pp. 177–183, Dec 2005.

[14] A. Greentree, J. Cole, A. Hamilton, and L. Hollenberg, "Coherent electronic transfer in quantum dot systems using adiabatic passage," *Phys. Rev. B*, vol. 70, p. 235317, Dec 2004.

[15] R. Rahman, S. H. Park, J. H. Cole, A. D. Greentree, R. P. Muller, G. Klimeck, and L. C. L. Hollenberg, "Atomistic simulations of adiabatic coherent electron transport in triple donor systems," *Phys. Rev. B*, vol. 80, p. 035302, Jul 2009.

[16] C. Hill, L. Hollenberg, A. Fowler, C. Wellard, A. Greentree, and H. Goan, "Global control and fast solid-state donor electron spin quantum computing," *Phys. Rev. B*, vol. 72, p. 45350, Jul 2005.

[17] C. D. Hill, E. Peretz, S. J. Hile, M. G. House, M. Fuechsle, S. Rogge, M. Y. Simmons, and L. C. Hollenberg, "A surface code quantum computer in silicon," *Sci. Adv.*, vol. 1, p. e1500707, Oct 2015.

[18] G. Tosi, F. A. Mohiyaddin, S. B. Tenberg, R. Rahman, G. Klimeck, and A. Morello, "Silicon quantum processor with robust long-distance qubit couplings," *arXiv:1509.08538*, 2015.

[19] V. Srinivasa, H. Xu, and J. M. Taylor, "Tunable spin-qubit coupling mediated by a multielectron quantum dot," *Phys. Rev. Lett.*, vol. 114, p. 226803, Jun 2015.

[20] L. Trifunovic, F. L. Pedrocchi, and D. Loss, "Long-distance entanglement of spin qubits via ferromagnet," *Phys. Rev. X*, vol. 3, p. 041023, Dec 2013.

[21] G. Tosi, F. A. Mohiyaddin, H. Huebl, and A. Morello, "Circuit-quantum electrodynamics with direct magnetic coupling to single-atom spin qubits in isotopically enriched 28si," *AIP Advances*, vol. 4, p. 087122, Aug 2014.

[22] X. Hu, Y. Liu, and F. Nori, "Strong coupling of a spin qubit to a superconducting stripline cavity," *Phys. Rev. B*, vol. 86, p. 035314, Jul 2012.

[23] S. Bose, "Quantum Communication through an Unmodulated Spin Chain," *Phys. Rev. Lett.*, vol. 91, p. 20, Nov 2003.

[24] M. Friesen, A. Biswas, X. Hu, and D. Lidar, "Efficient Multiqubit Entanglement via a Spin Bus," *Phys. Rev. Lett.*, vol. 98, p. 230503, Jun 2007.

[25] S. Oh, M. Friesen, and X. Hu, "Even-odd effects of heisenberg chains on long-range interaction and entanglement," *Phys. Rev. B*, vol. 82, p. 140403, Oct 2010.

[26] S. Oh, L.-A. Wu, Y.-P. Shim, J. Fei, M. Friesen, and X. Hu, "Heisenberg spin bus as a robust transmission line for quantum-state transfer," *Phys. Rev. A*, vol. 84, p. 022330, Aug 2011.

[27] S. Oh, Y.-P. Shim, J. Fei, M. Friesen, and X. Hu, "Effect of randomness on quantum data buses of heisenberg spin chains," *Phys. Rev. B*, vol. 85, p. 224418, Jun 2012.

[28] H. Bethe, "Zur theorie der metalle," *Zeitschrift fr Physik*, vol. 71, no. 3-4, pp. 205–226, 1931.

[29] F. Meier, J. Levy, and D. Loss, "Quantum computing with spin cluster qubits," *Phys. Rev. Lett.*, vol. 90, p. 047901, Jan 2003.

[30] J. R. Petta, A. C. Johnson, J. M. Taylor, E. A. Laird, A. Yacoby, M. D. Lukin, C. M. Marcus, M. P. Hanson, and A. C. Gossard, "Coherent Manipulation of Coupled Electron Spins in Semiconductor Quantum Dots," *Science*, vol. 309, pp. 2180–2184, Sep 2005.

[31] S. Oh, Y.-P. Shim, J. Fei, M. Friesen, and X. Hu, "Resonant adiabatic passage with three qubits," *Phys. Rev. A*, vol. 87, p. 022332, Feb 2013.

[32] G. Feher, "Electron Spin Resonance Experiments on Donors in Silicon. I. Electronic Structure of Donors by the Electron Nuclear Double Resonance Technique," *Phys. Rev.*, vol. 114, pp. 1219–1244, Jun 1959.

[33] M. Steger, T. Sekiguchi, A. Yang, K. Saeedi, M. E. Hayden, M. L. W. Thewalt, K. M. Itoh, H. Riemann, N. V. Abrosimov, P. Becker, and et al., "Optically-detected NMR of optically-hyperpolarized 31P neutral donors in 28Si," *J. Appl. Phys.*, vol. 109, no. 10, p. 102411, 2011.

[34] B. Koiller, X. Hu, and S. Das Sarma, "Exchange in Silicon-Based Quantum Computer Architecture," *Phys. Rev. Lett.*, vol. 88, p. 027903, Dec 2001.

[35] D. Jamieson, C. Yang, T. Hopf, S. Hearne, C. Pakes, S. Prawer, M. Mitic, E. Gauja, S. Andresen, F. Hudson, et al., "Controlled shallow single-ion implantation in silicon using an active substrate for sub-20-keV ions," *Appl. Phys. Lett.*, vol. 86, p. 202101, Oct 2005.

[36] J. F. Ziegler, M. Ziegler, and J. Biersack, "SRIM : The stopping and range of ions in matter (2010)," *Nucl. Instrum. Meth. B*, vol. 268, p. 1818, Jun 2010.

[37] G. Jacob, K. Groot-Berning, S. Wolf, S. Ulm, L. Couturier, S. T. Dawkins, U. G. Poschinger, F. Schmidt-Kaler, and K. Singer, "Microscopy with a deterministic single ion source," *arXiv:1512.00347*, 2015.

[38] M. J. Calderón, B. Koiller, X. Hu, and S. Das Sarma, "Quantum control of donor electrons at the Si-SiO2 interface," *Phys. Rev. Lett.*, vol. 96, p. 096802, Mar 2006.

[39] F. A. Mohiyaddin, *Designing a Large Scale Quantum Computer with Classical and Quantum Simulations*. PhD thesis, University of New South Wales, Australia, 2014.

[40] Outside the [100] crystallographic axis, the exchange coupling between donor electrons in silicon exhibits a strong oscillatory dependence with donor separation due to valley interference[34].

[41] W. Lim, F. Zwanenburg, H. Huebl, M. Möttönen, K. Chan, A. Morello, and A. Dzurak, "Observation of the single-electron regime in a highly tunable silicon quantum dot," *Appl. Phys. Lett.*, vol. 95, no. 24, p. 242102, 2009.

[42] A. L. Saraiva, M. J. Calderón, X. Hu, S. Das Sarma, and B. Koiller, "Physical mechanisms of interface-mediated intervalley coupling in Si," *Phys. Rev. B*, vol. 80, p. 081305, Aug 2009.

[43] A. Laucht, J. T. Muhonen, F. A. Mohiyaddin, R. Kalra, J. P. Dehollain, S. Freer, F. E. Hudson, M. Veldhorst, R. Rahman, G. Klimeck, K. M. Itoh, D. N. Jamieson, J. C. McCallum, A. S. Dzurak, and A. Morello, "Electrically controlling single-spin qubits in a continuous microwave field," *Sci. Adv.*, vol. 1, p. e1500022, Apr 2015.

[44] P. Harvey-Collard, N. T. Jacobson, M. Rudolph, J. Dominguez, G. A. T. Eyck, J. R. Wendt, T. Pluym, J. K. Gamble, M. P. Lilly, M. Pioro-Ladrière, *et al.*, "Nuclear-driven electron spin rotations in a single donor coupled to a silicon quantum dot," *arXiv:1512.01606*, 2015.

[45] M. Urdampilleta, A. Chatterjee, C. C. Lo, T. Kobayashi, J. Mansir, S. Barraud, A. C. Betz, S. Rogge, M. F. Gonzalez-Zalba, and J. J. Morton, "Charge dynamics and spin blockade in a hybrid double quantum dot in silicon," *Phys. Rev. X*, vol. 5, p. 031024, Aug 2015.

[46] C. J. Wellard, L. C. L. Hollenberg, F. Parisoli, L. M. Kettle, H.-S. Goan, J. A. L. McIntosh, and D. N. Jamieson, "Electron exchange coupling for single-donor solid-state spin qubits," *Phys. Rev. B*, vol. 68, p. 195209, Nov 2003.

[47] Y. E. Wang, A. Tankasala, L. C. Hollenberg, G. Klimeck, M. Y. Simmons, and R. Rahman, "Engineering inter-qubit exchange coupling between donor bound electrons in silicon," *arXiv:1507.08009*, 2015.

[48] R. Rahman, S. H. Park, T. B. Boykin, G. Klimeck, S. Rogge, and L. C. L. Hollenberg, "Gate-induced g-factor control and dimensional transition for donors in multivalley semiconductors," *Phys. Rev. B*, vol. 80, p. 155301, Oct 2009.

[49] F. A. Mohiyaddin, R. Rahman, R. Kalra, G. Klimeck, L. C. L. Hollenberg, J. J. Pla, A. S. Dzurak, and A. Morello, "Noninvasive Spatial Metrology of Single-Atom Devices," *Nano Lett.*, vol. 13, pp. 1903–1909, May 2013.

[50] L. Hollenberg, A. Greentree, A. Fowler, and C. Wellard, "Two-dimensional architectures for donor-based quantum computing," *Phys. Rev. B*, vol. 74, p. 045311, Jul 2006.

[51] A. Morello, C. Escott, H. Huebl, L. Willems van Beveren, L. Hollenberg, D. Jamieson, A. Dzurak, and R. Clark, "Architecture for high-sensitivity single-shot readout and control of the electron spin of individual donors in silicon,"

[52] R. Kalra, A. Laucht, C. D. Hill, and A. Morello, "Robust two-qubit gates for donors in silicon controlled by hyperfine interactions," *Phys. Rev. X*, vol. 4, p. 021044, Jun 2014.

[53] T. Yuge, S. Sasaki, and Y. Hirayama, "Measurement of the noise spectrum using a multiple-pulse sequence," *Phys. Rev. Lett.*, vol. 107, p. 170504, Oct 2011.

[54] L. Viola, E. Knill, and S. Lloyd, "Dynamical decoupling of open quantum systems," *Phys. Rev. Lett.*, vol. 82, no. 12, p. 2417, 1999.

[55] G. Klimeck, S. S. Ahmed, H. Bae, N. Kharche, R. Rahman, S. Clark, B. Haley, S. Lee, M. Naumov, H. Ryu, F. Saied, M. Prada, M. Korkusinski, and T. B. Boykin, "Atomistic simulation of realistically sized nanodevices using NEMO 3-D - Part I: Models and benchmarks," *IEEE Trans. Electron. Dev.*, vol. 54, pp. 2079–2089, Sep 2007.

[56] G. Klimeck, S. S. Ahmed, N. Kharche, M. Korkusinski, M. Usman, M. Prada, and T. B. Boykin, "Atomistic simulation of realistically sized nanodevices using NEMO 3-D - Part II: Applications," *IEEE Trans. Electron. Dev.*, vol. 54, pp. 2090–2099, Sep 2007.

[57] J. Slater, *Quantum Theory of Molecules and Solids: Symmetry and energy bands in crystals.* International series in pure and applied physics, McGraw-Hill, 1965.

[58] C. J. Wellard and L. C. L. Hollenberg, "Donor electron wave functions for phosphorus in silicon: Beyond effective-mass theory," *Phys. Rev. B*, vol. 72, p. 085202, Aug 2005.

[59] R. Rahman, *Stark Tuning of Electronic Properties of Impurities for Quantum Computing Applications.* PhD thesis, Purdue University, USA, 2009.

[60] A. Laucht, R. Kalra, J. T. Muhonen, J. P. Dehollain, F. A. Mohiyaddin, F. Hudson, J. C. McCallum, D. N. Jamieson, A. S. Dzurak, and A. Morello, "High-fidelity adiabatic inversion of a 31P electron spin qubit in natural silicon," *Appl. Phys. Lett.*, vol. 104, p. 092115, Mar 2014.

Phys. Rev. B, vol. 80, p. 81307, Aug 2009.